Plasma Assisted Surface Nitridation of Proton Intercalatable WO_3 for Efficient Electrocatalytic Ammonia Synthesis

Zhiyuan Zhang [a], *Christopher Kondratowicz* [b], *Jacob Smith* [c], *Pavel Kucheryavy* [a], *Junjie Ouyang* [a], *Yijie Xu* [b], *Sophia Kurdziel* [d], *Eddie Tang* [b, e], *Micheal Adeleke* [a, f], *Aditya Dilip Lele* [g], *John Mark Martirez* [d], *Miaofang Chi* [c, h], *Yiguang Ju* [b, d*,] *Huixin He* [a]*

[a] Department of Chemistry, Rutgers, the State University of New Jersey, Newark, New Jersey 07102, United States

[b] Department of Mechanical and Aerospace Engineering, Princeton University, Princeton, New Jersey 08544, United States

[c] Center for Nanophase Materials Sciences, Oak Ridge National Laboratory, Oak Ridge, Tennessee 37831, United States

[d] Applied Materials and Sustainability Sciences, Princeton Plasma Physics Laboratory, Princeton, New Jersey 08543, United States

[e] Montgomery High School, Skillman, New Jersey 08558, United States

[f] Science Park High School, Newark, New Jersey 07103, United States

[g] Department of Mechanical Engineering, Rowan University, Glassboro, New Jersey 08028, United States

[h] Thomas Lord Department of Mechanical Engineering & Materials Science, Duke University, Durham, North Carolina 27708, United States

Abstract:

Electrocatalytic nitrogen reduction (eNRR) offers a green pathway for NH_3 production from N_2 and H_2O under ambient conditions. Transition metal oxynitrides (TMO_xN_y) are among the most promising catalysts but face challenges in achieving high yield and faradaic efficiency (FE). This work develops a hybrid WO_xN_y/WO_3 catalyst with a unique heterogeneous interfacial complexion (HIC) structure. This design enables *in situ* generation and delivery of highly active hydrogen atoms (H^*) in acidic electrolytes, promoting nitrogen hydrogenation and formation of nitrogen vacancies (Nv) on the WO_xN_y surface. This significantly enhances the selectivity of eNRR for NH_3 synthesis while suppressing hydrogen evolution reaction (HER). A simple two-step fabrication process—microwave hydrothermal growth followed by plasma-assisted surface nitridation—was developed to fabricate the designed catalyst electrode, achieving an NH_3 yield of 3.2×10^{-10} $mol\cdot cm^{-2}\cdot s^{-1}$ with 40.1% FE, outperforming most TMN/TMO_xN_y electrocatalysts. Multiple control experiments confirm that the eNRR follows a HIC-enhanced Mars-van Krevelen (MvK) mechanism.

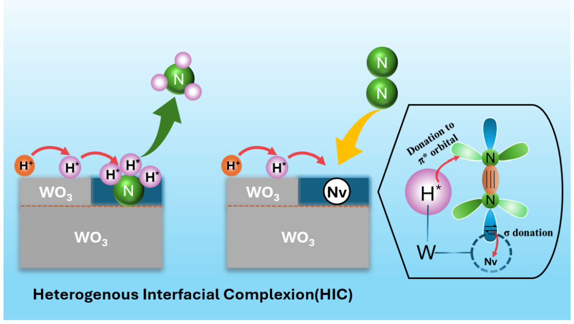

Ammonia (NH_3) has traditionally been used as a fertilizer and a key chemical in chemical industries. More recently, NH_3 has emerged as a promising hydrogen (H_2) carrier for green power storage and generation, due to its higher energy density, lower storage and transport costs, and lower flammability compared to H_2.[1, 2] However, the current production method, the Haber-Bosch (H-B) process operates under high temperatures (~500 °C) and pressures (~250 atm) and relies on H_2 produced from fossil fuels. This makes it not only energy- and CO_2-intensive, but also highly centralized, limiting its integration with intermittent and location specific renewable electricity.[3, 4] To address these challenges, it is essential to develop efficient, distributed, and electrified methods to produce green NH_3 directly from water (H_2O) using renewable electricity.[5, 6]

To overcome the challenges of the H-B process and enable electrified synthesis of NH_3, plasma-catalytic NH_3 synthesis from N_2 and water (H_2O) or H_2 has been pursued.[7-9] Plasma catalysis offers non-equilibrium reaction pathways for NH_3 synthesis by utilizing active atomic nitrogen (N) and vibrationally excited nitrogen ($N_2(v)$), as well as catalyst surface nitridation.[7, 8, 10] However, the energy efficiency of plasma-assisted NH_3 synthesis remains significantly lower (8.7 g-NH_3/kWh) than that of the H-B process (500 g-NH_3/kWh).[11, 12] Additionally, when H_2O is used as the hydrogen source in plasma, undesired byproducts such as NO_x and H_2O_2 can be generated.[10] Electrocatalytic nitrogen reduction reaction (eNRR) allows green production of NH_3 from N_2 and H_2O under ambient conditions without the undesired pollutants and other harmful byproducts.[13] However, the practical implementation of eNRR for NH_3 production is impeded by the extremely low NH_3 yield and low Faradaic efficiency (FE) due to the high activation energy of inert N_2 molecules, and the overwhelming HER competition reaction.[14, 15]

Transition metal nitrides (TMNs) and oxynitrides (TMO_xN_y) have emerged as promising catalysts for eNRR due to their distinctive structural properties, which enable nitrogen reduction through the Mars-van Krevelen (MvK) catalytic pathway with much lower energy barrier compared to N adsorbate reduction via direct proton-coupled electron transfer (PCET).[16-20] In MvK pathway, ammonia (NH_3) is initially produced by hydrogenating lattice nitrogen (N) atoms on the surface of TMNs or TMO_xN_y. This process significantly reduces the energy barrier for NH_3 production as it avoids the need for direct activation and cleavage of the N≡N triple bond in N_2.[14] Desorption of these NH_3 molecules generate nitrogen vacancies (Nv) on the catalyst surface, which subsequently act as the catalytic sites, adsorbing and activating the dissolved N_2 from the electrolyte and completing the catalytic cycles. Although the subsequent steps still require the cleavage of the N≡N triple bond, it is noteworthy that the nitrogen vacancies not only provide unsaturated coordination sites that facilitate N_2 adsorption but also efficiently activate the adsorbed N_2 molecules by accommodating the lone pair of electrons from N_2 due to the electron-deficient nature of the vacancies.[21] Importantly, the electron-deficient nature of nitrogen vacancies selectively favors the adsorption and activation of N_2 over H^+, thereby minimizing competition from hydrogen evolution reaction (HER).[16, 17] The concurrent high activity and selectivity for eNRR stands in stark contrast to oxygen vacancies (Ov) on transition metal oxides (TMO).[22]

Recent studies demonstrated that transition metal oxynitrides (TMO_xN_y) exhibit higher catalytic activity and better stability than that of TMN based catalysts.[2, 17, 18, 22, 23] Nevertheless, the NH_3 yield for both TMO_xN_y and TMN based catalysts is still far lower for practical applications. Considerable efforts have been made to understand the reasons behind the observed low eNRR activities.[22, 24] It is commonly accepted that Nv generation/regeneration are considered as the rate determining step of the MvK mechanism.[17, 22, 25] For Nv-free TMN and TMO_xN_y catalysts, the initial hydrogenation of lattice nitrogen is widely regarded as the most challenging step.[22, 24-27] For Nv-rich TMN and TMO_xN_y catalysts, the desorption of the generated NH_3 becomes a critical factor in completing the Nv regeneration cycle.[21, 24]

To promote Nv generation, the Hosono group developed nickel-loaded lanthanum nitride (LaN) for high-temperature thermal catalytic hydrogenation of N_2 for NH_3 synthesis.[27] In this catalyst design, nickel clusters efficiently dissociate H_2 into highly active H^* at high temperatures, which then migrates to the LaN, significantly facilitating nitrogen atom hydrogenation and promoting the formation of nitrogen vacancies (Nv) on the LaN surface. In the electrocatalytic field, Zhang's group has demonstrated the crucial role of H^* in facilitating Nv generation on copper nitride (Cu_3N) at room temperatures.[28] Their catalyst design employed a novel graphdiyne support to electrochemically generate H atoms. The coexistence of H atoms and Nv significantly facilitated the electrocatalytic reduction of nitrate (NO_3^-). However, leveraging H^* to induce Nv formation in TMN/TMO_xN_y systems for enhanced electrocatalytic N_2 reduction to NH_3 remains unexplored.

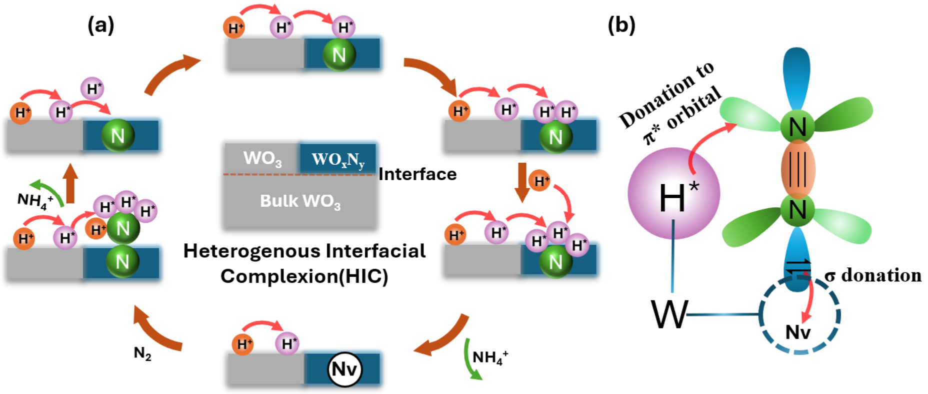

Scheme 1. (a) Schematic illustration showing how the designed WO_xN_y/WO_3 electrocatalyst with a HIC structure enables in-situ generation of H^* via proton intercalation to promote the hydrogenation of lattice nitrogen (N) in WO_xN_y, leading to the formation of nitrogen vacancies (Nv) and the creation of new catalytic centers for enhanced eNRR. (b) Schematic representation of the orbital interaction between N_2 and the new catalytic center, which is highly active and selective for N_2 absorption and activation.

In this work, we design WO_xN_y/WO_3 hybrid electrochemical catalysts featuring a unique heterogeneous interfacial complexion (HIC) structure[29] **(Scheme 1a)**. We hypothesize that the HIC structure enables in-situ generation of H^* via proton intercalation, enhancing eNRR through a HIC enhanced Mars–van Krevelen (MvK) mechanism. WO_xN_y is selected for its eNRR activity and stability against chemical decomposition, outperforming tungsten nitride (WN) due to its elevated N_{2p} orbital near the Fermi level (E_F).[2, 22, 30] Meanwhile, WO_3 facilitates *in-situ* proton (H^+) intercalation ($WO_3 + xH^+ + xe^- \rightleftharpoons H_xWO_3$), generating mobile, active, and relatively long-lived H atoms (in the form of weakly bound hydrogen, denoted as W-H^*) in acidic electrolyte.[31-33] This HIC architecture ensures that WO_3 retains its proton intercalation capability along the electron/proton transport pathway. We further hypothesize that W-H* generated at the WO_xN_y/WO_3 interface, or migrated from WO_3 domains to this interface, promotes hydrogenation of lattice nitrogen in WO_xN_y to form NH_3. The abundance of H^+ ions in the acidic electrolyte facilitates the protonation and desorption of the produced NH_3 from the WO_xN_y catalyst surface, facilitating generation of nitrogen vacancies (Nv). In the subsequent steps, these Nv sites, combined with the continuous H^* supply at neighboring W centers, form new catalytic sites, as illustrated in **Scheme 1b.** The newly formed catalytic sites at the WO_xN_y/WO_3 interface facilitate bidirectional electron transfer, a critical requirement for efficient N_2 activation, thereby significantly enhancing activation capability.[34] Specifically, the Nv preferentially adsorbs electron donor like N_2 over H^+ due to their electron-deficient nature,[21] allowing Nv to accept the lone pair electrons from adsorbed N_2. Meanwhile, the H^* on adjacent W sites donates electrons into the antibonding π orbitals (π^*) of the adsorbed N_2, weakening the $N\equiv N$ triple bond and significantly enhancing its activation.[35, 36] This cooperative interaction boosts N_2 activation, increasing selective ammonia synthesis while suppressing the competing hydrogen evolution reaction (HER).

To fabricate the WO_xN_y/WO_3 hybrid catalysts with the proposed HIC architecture, a novel two-step process was developed. This process involves the facile microwave-assisted hydrothermal growth of a WO_3 nanosheet array, followed by a surface nitridation process achieved through non-equilibrium hydrogen/nitrogen plasma-assisted treatment. As illustrated in **Scheme 2(a)** and **(b),** a predominantly vertically aligned WO_3 nanosheet array is first grown on highly conductive carbon cloth with a hydrophobic microporous layer (MPL) using a facile microwave-assisted hydrothermal method. This is followed by a plasma-assisted surface nitridation process to convert part of the outer layer of WO_3 into

WO_xN_y while preserving the bulk WO_3 structure. Upon optimization, the developed WO_xN_y/WO_3 catalyst electrode achieved an impressive NH_3 yield rate of 3.2×10^{-10} $mol \cdot cm^{-2} \cdot s^{-1}$ at -0.15 V vs. RHE in an acidic H_2SO_4 electrolyte (pH = 2). This yield is approximately eight times higher than that of a single-layer 2D W_2N_3 catalyst, which theoretically possesses significantly more catalytic centers due to its single-layer structure.[21] Remarkably, this high yield is accompanied by an unprecedented Faradaic efficiency (FE) of 40.1%, the highest reported for any transition metal nitride (TMN) or transition metal oxynitride (TMO_xN_y)-based catalyst, which typically exhibit FE values below 15%.[17, 21, 22, 37-41]

The detailed procedures for the growth of WO_3 nanosheet array on a piece of highly conductive carbon cloth with a microporous layer (MPL) were described in **supplementary S1**. This approach significantly shortens the reaction time to just 15 minutes, a marked improvement compared to the 24 - 48 hours required by conventional hydrothermal methods.[42] Notably, this synthesis method enables us to directly grow WO_3 on the hydrophobic MPL side of the carbon cloth.

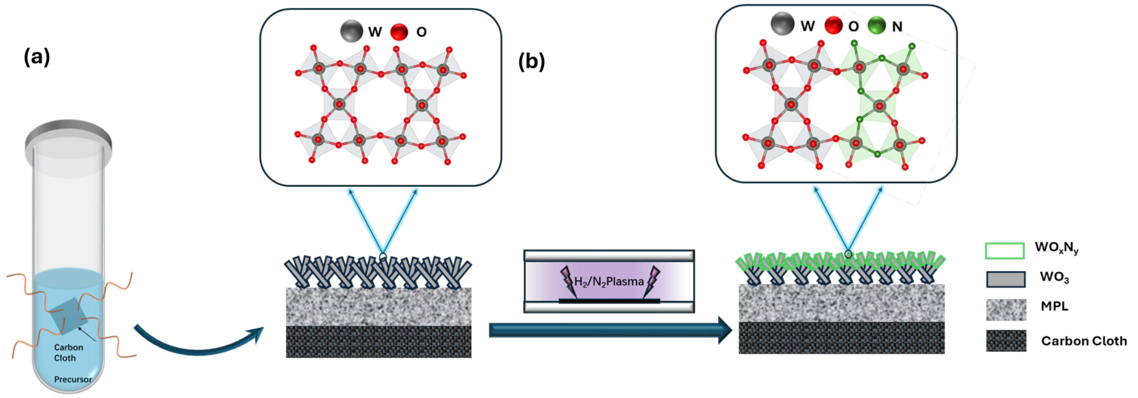

Scheme 2. Schematic illustration of the two-step process for preparing largely vertically aligned WO_xN_y/WO_3 with the designed HIC architecture on a piece of carbon cloth with a

hydrophobic MPL. (a) microwave-assisted hydrothermal growth of WO_3 nanosheet array on the MPL of carbon cloth; (b) surface nitridation of the WO_3 nanosheets via non-equilibrium plasma to form WO_xN_y/WO_3, while leaving the WO_3 crystal structure and the underneath hydrophobic MPL intact, therefore the as-prepared WO_xN_y/WO_3 hybrid catalyst electrodes were directly employed as gas diffusion electrodes for eNRR.

Scanning electron microscope (SEM) was used to characterize the structure of the WO_3 nanostructures. **Figures 1a** shows the nanosheet-like morphology of the as-prepared WO_3, with the nanosheets predominantly aligned vertically but exhibiting random orientations. Each individual nanostructure appears as a thin, platelet-like crystal measuring a few tens to hundreds of nanometers in thickness and extending laterally on the order of hundreds of nanometers to a few micrometers. **Figure 1b** further reveals that each nanosheet is composed of an assembly of nanocrystals, suggesting a high surface area, which is highly beneficial for catalytic applications. The crystal structure of the WO_3 was characterized with powder X-ray diffraction (PXRD). As shown in **Figure 1c**, the diffraction peaks of the as-prepared WO_3 align well with hexagonal WO_3 (h-WO_3, JCPDS No. 33-1387).

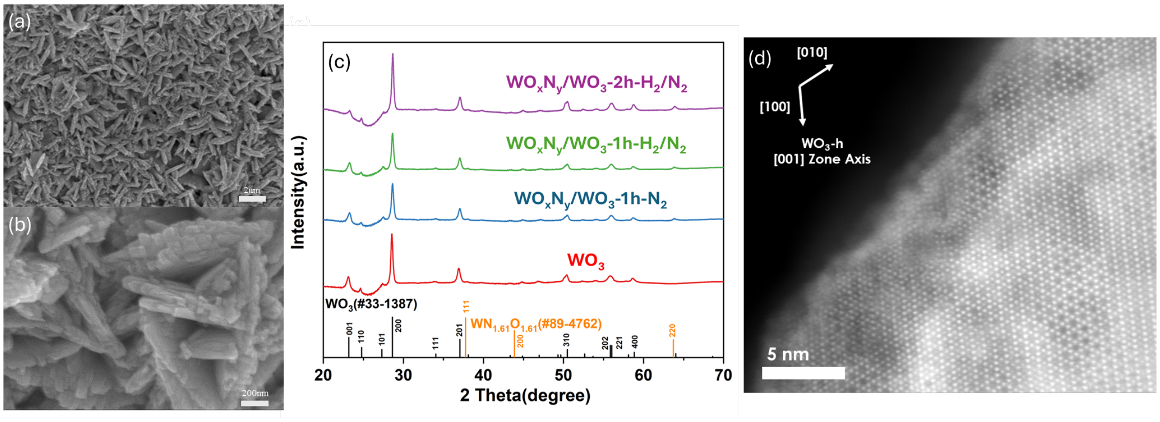

Figure 1. (a and b) SEM images of the h-WO_3 nanosheets at different magnifications, which directly grow on a piece carbon cloth with a hydrophobic microporous layer. (c) PXRD patterns of h-WO_3 before and after plasma-assisted nitridation (d) Surface reconstruction of h-WO_3 after plasma treatment. Atomic-resolution HAADF-STEM imaging shows that the hexagonal structure of h-WO_3 remains intact, with a thin amorphous layer forming on the surface.

To achieve surface nitridation of the h-WO_3 nanosheet array while preserving the underlying WO_3 crystal structure and the MPL layer on the carbon cloth, a novel room-temperature, non-equilibrium plasma-assisted surface nitridation approach was developed. This method utilizes a hydrogen/nitrogen mixture plasma, enabling the direct fabrication of the hybrid WO_xN_y/WO_3 catalyst electrode with the designed HIC architecture at room temperature. This approach ensures precise control over nitridation while maintaining the structural integrity and electronic properties essential for efficient proton and electron transport. Briefly, the synthesized WO_3 nanosheets on carbon cloth described above were used as the precursor, directly located in a H_2/N_2 dielectric barrier discharge (DBD) plasma chamber for the surface nitridation. Various plasma treatment conditions, including N_2 plasma for 1 hour, first H_2 plasma for half hour, followed by N_2 plasma for 1 hour, H_2/N_2 (1:4) plasma for 1 hour, and H_2/N_2 plasma for 2 hours, were tested to optimize the surface nitridation. The resulting hybrid WO_xN_y/WO_3 catalyst electrode was accordingly named as WO_3-N_2-1h, WO_3-H_2-0.5h-N_2-1h, WO_3-H_2/N_2-1h, and WO_3-H_2/N_2-2h, respectively.

SEM and PXRD were also used to study their morphology and crystal structural change after plasma treatment. By comparing **Figure S1a-c** (SEM as-prepared WO_3) **to Figure S1d-f** (SEM post-nitridation)**,** the WO_3 nanostructures retain their morphology without significant changes under the applied plasma nitridation conditions. Note that a new peak at 63.6° with very low intensity appears on the PXRD spectra **(Figure 1c)** with WO_3-H_2/N_2-2h having the highest intensity, indicating the formation of WO_xN_y (JCPDS No. 89-4762). However, the diffraction peaks of h-WO_3 remained largely unchanged across all the plasma nitridation conditions studied. This result suggests that the crystal structure of h-WO_3 remains largely intact. To further investigate the atomic-scale structural changes of h-WO_3 after nitridation, high-angle annular dark-field scanning transmission electron microscopy (HAADF-STEM) was utilized to image the WO_3-H_2/N_2-2h catalyst, which exhibited the highest intensity of the new peak at 63.6° in the PXRD spectrum (**Figure 1c**). As shown in **Figure 1d**, the well-defined hexagonal crystal structure of h-WO_3 was largely preserved, consistent with the bulk PXRD studies. However, a very thin (1–2 nm) amorphous surface layer appeared, which likely associated with the formation of WO_xN_y species, as confirmed by electron energy-loss spectroscopy (EELS). As shown in **Figure S2**, minimal nitrogen signals are observed in the bulk WO_3, whereas a nitrogen-rich region is detected within the amorphous layer near the surface.

All these structural characterizations demonstrated that the WO_3 surface was selectively nitridated while preserving the bulk crystal structure, leading to the formation of the designed heterogeneous interfacial complexion (HIC) structure—an achievement that is difficult to realize using conventional high-temperature annealing nitridation methods.[43] First, the h-WO_3 crystal structure represents an intermediate phase within the WO_3 family. At elevated temperatures, around 400 °C, h-WO_3 transitions into monoclinic WO_3 (m-WO_3), the most thermodynamically stable form of WO_3.[44, 45] In addition, even when using m-WO_3 as a starting material for nitridation, a significant degradation of its crystal structure at 500 °C occurs—this is the temperature at which WO_xN_y/WN begins to emerge.[43, 46] These findings highlight a key advantage of the non-equilibrium plasma nitridation approach over traditional thermal nitridation methods,[47] i.e., its ability to achieve surface nitridation while preserving the underlying WO_3 crystal structure, which is crucial for maintaining proton intercalation and electronic transport properties.

To gain insight into the composition and electronic structure of the amorphous WO_xN_y surface layer of the HIC structure, X-ray photoelectron spectroscopy (XPS), a surface-sensitive technique, was performed. As expected, there is no detectable N in the as-prepared h-WO_3 sample, as shown in **Figure 2a.** After plasma-assisted surface nitridation, a distinct nitrogen signal is detected on the surface of all samples, further confirming the successful incorporation of nitrogen into the WO_3 nanostructures. However, high-resolution XPS analysis **(Figure 2b)**, as described below, reveals that none of the samples exhibit W^{3+}-related peaks, indicating that the nitridation conditions did not lead to the formation of WN domains. This suggests that the nitridated surface likely consists of WO_xN_y rather than WN.[43] As shown in table **S1**, the surface composition was further quantified based on the integrated peak areas in their respected XPS spectrum. The WO_3-H_2/N_2-2h sample exhibits the highest nitrogen content of 14.3 at%, which remains significantly lower than that of any known tungsten oxynitride phases.[48] This suggests that the amorphous HIC layer observed in **Figure 1d** is not composed solely of a uniform WO_xN_y phase. Instead, it likely consists of a heterogeneous mixture of WO_3 and WO_xN_y domains, as schematically illustrated in **Scheme 1**.

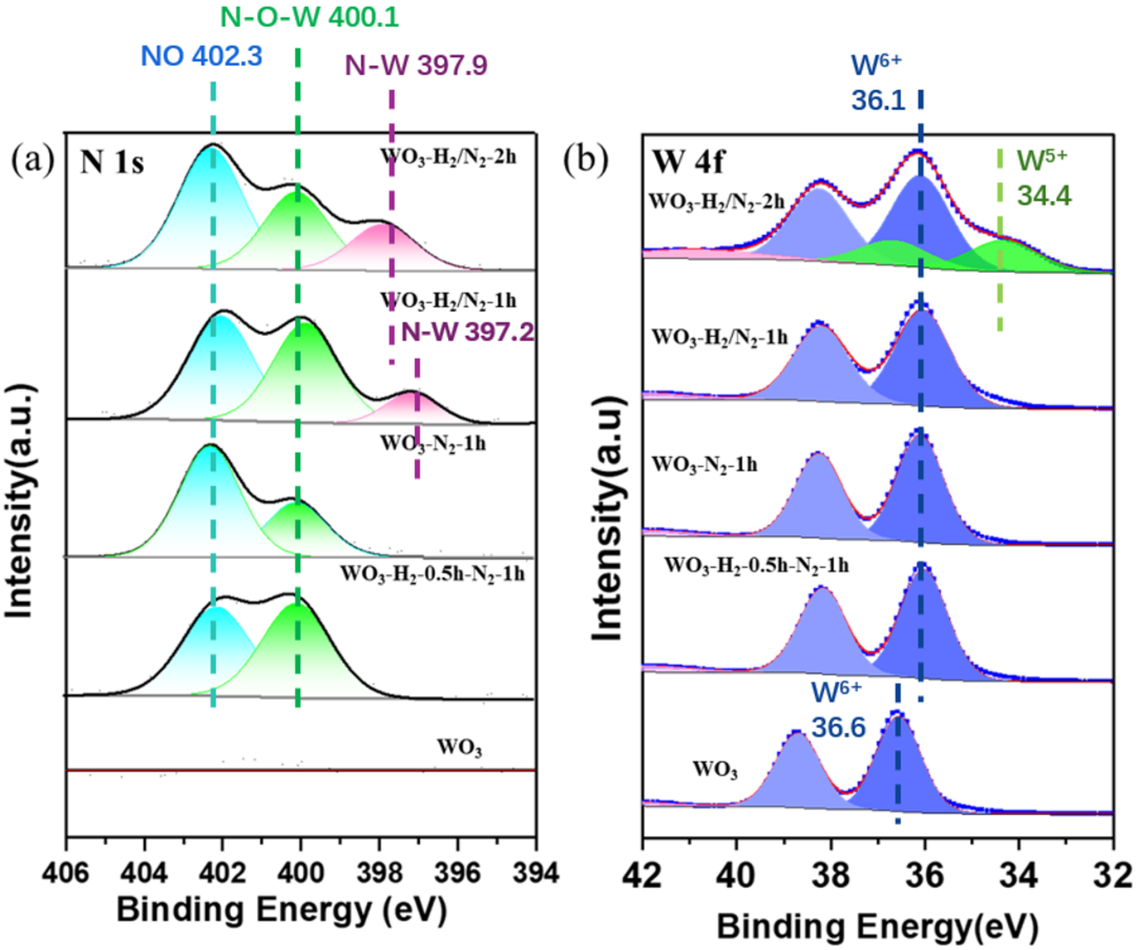

Figure 2. High-resolution XPS spectra of h-WO_3 before and after plasma nitridation under different conditions: (a) N 1s, (b) W 4f.

To carefully study the chemical configuration of the N in the HIC structures, high-resolution N 1s spectrum was collected and the N peaks were carefully deconvoluted. As shown in **Figure 2a,** the high-resolution N 1s peaks for WO_3-H_2/N_2-2h and WO_3-H_2/N_2-1h samples can be deconvoluted into three distinct peaks, whereas for the WO_3-N_2-1h and WO_3-H_2-0.5h-N_2-1h samples, only two peaks were observed. Based on the previous literatures, the peaks in the range of 397.9-397.0 eV and 402.3 eV are assigned to W-N and N-O bonds, respectively.[43] The assignment for the peak at 400.1 eV was inconsistent across studies. Some reports assigned it to N-W-O bond or to nitrogen vacancy (Nv) related.[43, 49, 50] Nevertheless, the presence of the W-N peak suggests the successful formation of oxynitride species. Notably, this peak appears only in samples treated with an H_2/N_2 plasma and is absent in N_2 plasma-treated samples. Additionally, sequential H_2 plasma treatment followed by N_2 plasma treatment did not produce the same effect, suggesting that NH_x radicals formed in the H_2/N_2 plasma may play a role in accelerating surface nitridation.[51, 52] Furthermore, the intensity of the W-N peak in the WO_3-H_2/N_2-1h sample is significantly lower than in the WO_3-H_2/N_2-2h sample, indicating that longer treatment times facilitate more N-W bond formation. Despite this, all the samples show high peak densities corresponding to N-O bonds and N-W-O/Nv-related bonds. Interestingly, the peak associated with N-W-O/Nv-related bonds in the WO_3-H_2/N_2-1h sample is even higher than in the WO_3-H_2/N_2-2h sample. These results suggest a plasma nitridation pathway in which N-O and N-W-O/Nv-related species serve as intermediates in the formation of N-W bonds.

The high-resolution W 4f spectrum shows characteristic peaks at 38.8 eV and 36.6 eV, which correspond to W^{6+} in the as-prepared WO_3 sample (**Figure 2b,** bottom curve). After plasma-assisted surface nitridation, a negative shift of approximately 0.5 eV was observed for the WO_3-H_2/N_2-2h, WO_3-H_2/N_2-1h, and WO_3-N_2-1h samples, indicating a slight reduction in the oxidation state of W upon nitridation, which is consistent with the literatures.[13, 43] Two additional peaks at even lower binding energy (36.6 eV and 34.4 eV) were observed for the WO_3-H_2/N_2-2h sample, which can be assigned to W^{5+} species.[13, 53] These results suggest that the electron density of the W centers in the nitridated samples is higher than that in the parent h-WO_3, with WO_3-H_2/N_2-2h exhibiting the highest electron density.[53] It is reported that a higher electron density of the W centers facilities the formation of W-H* species.[33] As we proposed, the facile formation of W-H* species play a crucial role in promoting N hydrogenation, facilitating the formation of nitrogen vacancies (Nv) in the catalyst, and accelerating the eNRR catalytic cycles in WO_xN_y-based catalysts (**Scheme 1**). Furthermore, the coexistence of WO_3 domains and the unique HIC architecture of the catalyst is expected to sustain proton intercalation, ensuring the continuous generation and delivery of active H* species to the WO_xN_y regions for the formation of W-H* **(Scheme 1a)**. As a result, significantly enhanced eNRR activity is anticipated.

We then evaluate the eNRR performance of the WO_xN_y/WO_3 hybrid catalyst electrodes and investigate the correlation between their structural characteristics and catalytic activity. The eNRR was conducted in an acidic electrolyte (H_2SO_4, pH = 2) using a custom-designed N_2 flow electrolysis cell, as shown in **Scheme S1a**. In this configuration, the WO_xN_y/WO_3 hybrid catalysts were directly employed as gas diffusion electrodes (GDEs) to address the low solubility of N_2 in water (0.71 mg/L).[54] The electrolyte in the working electrode (WE) side of the cell was collected for quantification of ammonium (NH_4^+) and possible hydrazine (N_2H_4) byproduct using the indophenol blue UV-Vis spectroscopy method, the Watt-Chrisp method, and NMR spectroscopy as detailed in **Sections S6-S8.** The NH_3 yield rate and Faradic efficiency (FE) for the nitrogen-ammonia conversion were calculated as detailed in **Section S9**.

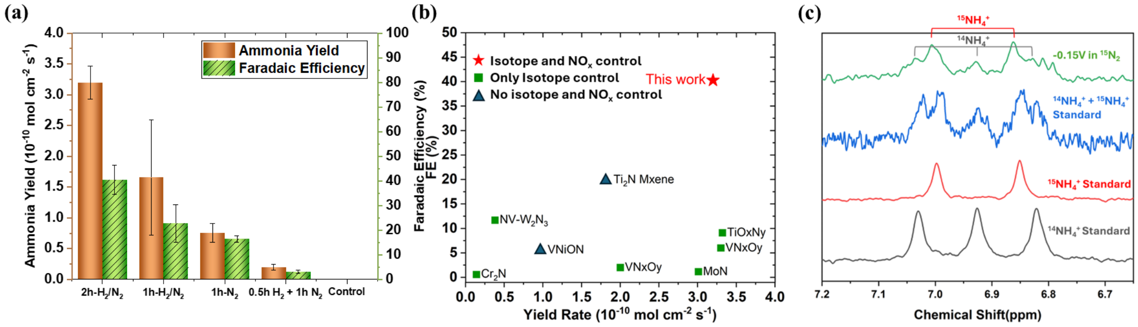

Figure 3. (a) Comparison of the eNRR performance of WO_3 with different plasma treatments under identical conditions (at -0.15 V vs RHE) in the first half hour. (b) Comparison of eNRR performance of TMN and TMO_xN_y based catalysts. (c) ^1H nuclear magnetic resonance (NMR) spectra of the electrolyte after eNRR electrolysis on WO_3-H_2/N_2-2h under $^{15}N_2$ purging.

We first studied the NH_3 yield rate and Faradaic efficiency (FE) of the WO_3-H_2/N_2-2h sample, which contains the highest W-N, at different cathodic potentials. As shown in **Figure S3**, as the cathodic potential becomes more negative from -0.05 V to -0.25 V vs RHE, the steady-state electrolysis current increased, while the NH_3 yield rate initially increased and then decreased, peaking at -0.15 V vs RHE. However, the FE dropped from 56.6% at -0.05 V to 40.5%, and then drastically decreased to 12.2% at -0.25 V vs RHE. We attribute this drastic FE decrease to increased HER competition, as indicated by current fluctuations in the chronoamperometry curve for $t > 1300$ s, caused by H_2 gas bubbles that accumulate and then detach from the electrode surface (**Figure S3b**).[12] Based on these results, we compared the NH_3 yield rate and FE of other catalysts at -0.15 V vs RHE. It is also worth noting that the NH_3 yield rates were calculated based on the geometric area of catalyst electrodes, as their electrochemical surface areas (ECSAs), estimated via the double-layer capacitance (C_{dl}) method, were similar (detailed in **Section S10** and **Figure S4**). The NH_3 yield rate and FE of WO_3-H_2/N_2-1h are lower than those of WO_3-H_2/N_2-2h, which can be attributed to its reduced W-N content and the absence of W^{5+} species, as confirmed by the N 1s and W 4f XPS spectra. Similarly, the significantly lower performance of WO_3-N_2-1h and WO_3-H_2-0.5h-N_2-1h is due to the lack of W-N bonds. Among all the samples, WO_3-H_2/N_2-2h demonstrates the highest NH_3 yield rate of 3.2×10^{-10} $mol \cdot cm^{-2} \cdot s^{-1}$, accompanied by a FE of 40.1%. This enhanced performance correlates with the fact that WO_3-H_2/N_2-2h contains the highest number of W-N species and exhibits the highest electron density at the W centers, both of which facilitate the formation of W-H^* species, as discussed previously. Notably, this FE surpasses all previously reported values for transition metal nitride- and oxynitride-based catalysts in aqueous electrolytes, which typically exhibit FE values below 15% **(Figure 3b)**.[17, 21, 22, 37-41] The remarkably high FE of the WO_xN_y/WO_3 catalysts indicates significantly lower HER competition. This is especially worth mentioning because HER is generally more dominant in acidic electrolytes compared to alkaline electrolytes.[55-57]

To verify that the detected ammonia originates exclusively from electrocatalytic N_2 reduction—and not from false contributions such as NH_3 or NH_4^+ released from the carbon cloth (CC), electrolysis cell, electrolyte contamination, or the N_2 gas feed—two carefully designed control experiments were performed: (1) The direct use of the h-WO_3 nanosheet array grown on carbon cloth via the microwave hydrothermal method (without subsequent plasma nitridation) as the working electrode to perform electrolysis at -0.15 V versus RHE under N_2 flow, and (2) the use of the WO_3-H_2/N_2-2h as the working electrode to run electrolysis under N_2 flow but keeping the potential at open circuit potential (OCP). In both cases, no detectable NH_4^+ was produced as shown in **Figure 3a and S5a**. These results not only demonstrate that h-WO_3 alone is inactive for eNRR but also confirm that ammonia synthesis is exclusively driven by the electrochemical activity of the WO_xN_y/ WO_3 catalyst.

It has been reported that commercial N_2 gas may contain non-negligible amounts of NO_x and other impurities, which can be more readily catalytically reduced to NH_3, potentially leading to false positive results in NH_3 synthesis experiments.[22] To ensure that NO_x impurities in the N_2 feed did not contribute to the observed results, we followed the protocol developed by Douglas *et al.* to remove the possible NO_x in the N_2 feed [58] as illustrated in **Scheme S1b**. Specifically, prior to introducing onto the back side of the GDE working electrode, the feed N_2 gas was passed three purification traps to effectively eliminate any NO_x impurities in the gas feed: (1) a $KMnO_4$ oxidation trap to oxidize any NO_x present in the N_2 gas into soluble NO_3^-, (2) a KOH trap to remove the possibly formed NO_3^-, and (3) a 0.1 M H_2SO_4 solution to trap any residual NH_3 in the N_2 gas. As shown in **Figure S5b**, the NH_3 yield obtained after NO_x purification was approximately 8% lower than the yield achieved using only the NH_3 trap without NO_x purification. This difference falls within the experimental error range, confirming that under the conditions employed in this study, the observed NH_3 yield is genuine and not significantly affected by possible NO_x impurities in the N_2 feed. Additionally, no hydrazine (N_2H_4) was detected in the post-electrolysis electrolyte, as shown in Figure **S6**.

To further confirm that the detected NH_4^+ originates from the electrocatalytic reduction of the feed N_2 via the MvK mechanism, a ^{15}N isotopic labeling experiment was conducted using $^{15}N_2$ as the feed gas (**Section S8 and Scheme S2**). The resulting product was analyzed via ^1H NMR spectroscopy, taking advantage of the distinct characteristic features between $^{15}NH_4^+$ and $^{14}NH_4^+$ in NMR spectra to verify the nitrogen source of the NH_4^+ product. As shown in **Figure 3c,** the ^1H NMR spectrum of the electrolyte after eNRR electrolysis using the WO_3-H_2/N_2-2h catalyst with $^{15}N_2$ as the gas feed (top curve) displays five peaks. This spectrum closely matches a standard sample containing both $^{15}NH_4^+$ and $^{14}NH_4^+$. The two characteristic peaks at $\delta = 6.85$ and 6.99 ppm are attributed to $^{15}NH_4^+$, while the three peaks at $\delta = 6.82$, 6.93, and 7.03 ppm correspond to $^{14}NH_4^+$. The peak height for $^{15}NH_4^+$ peaks is much higher than those of $^{14}NH_4^+$ suggested that most of the detected NH_4^+ comes from electrocatalytic reduction of the $^{15}N_2$ feed.

The simultaneous detection of $^{15}NH_4^+$ and a small amount of $^{14}NH_4^+$ in ^{15}N isotope labeling experiments has been used as an indication of MvK mechanism as both lattice nitrogen on the catalyst surface and the N_2 feed contribute to nitrogen turnover during eNRR.[17] This is because the initial NH_3 generation originates from the hydrogenation of lattice nitrogen on TMN and TMO_xN_y-based electrocatalysts. This suggests that NH_3 can be produced at the start of electrolysis without the need for an external N_2 feed, distinguishing this process from direct proton-coupled electron transfer (PCET) of adsorbate nitrogen.[34] However, it is important to note that TMN and TMO_xN_y-based electrocatalysts can also generate NH_3 without an external N_2 feed through electrochemically driven decomposition, rather than by hydrogenation of surface lattice nitrogen under acidic conditions.[2] It has been reported that electrochemical-driven decomposition of TMN has led to false positives in discovering new electrocatalysts for eNRR.[22, 59-61] Therefore, the detection of $^{14}NH_4^+$ in the NMR does not yet confirm that the eNRR is proceeding via the MvK mechanism. Further evidence is required to demonstrate that $^{14}NH_4^+$ is not a result of electrochemical-driven decomposition of the catalyst in acidic electrolytes.

To determine whether the detected $^{14}NH_4^+$ originated from the hydrogenation of surface lattice nitrogen or from the electrochemically driven decomposition of the catalyst in acidic electrolytes—and thereby unambiguously confirm that the WO_xN_y/WO_3 catalyst follows the MvK mechanism during eNRR—a detailed XPS study of the catalyst after electrolysis was conducted. If the detected NH_3 was due to decomposition, a concurrent loss of N and W on the WO_xN_y surface would be expected.[2] On the other hand, if the detected $^{14}NH_4^+$ was originated from hydrogenation of the surface lattice N, no W loss should be observed. As shown in **Figure 4 and S7,** after electrolysis, W^{5+} in the catalyst was converted to W^{6+}, while the total W signal remained nearly unchanged, indicating minimal decomposition. This suggests that the $^{14}NH_4^+$ detected by NMR under N_2 purging originates from the initial hydrogenation of lattice nitrogen in WO_xN_y rather than from its decomposition. Taken together, all the experimental results confirm that the eNRR facilitated by the WO_3-H_2/N_2-2h catalyst follows a MvK mechanism. In this work, we refer to it as the HIC-enhanced MvK mechanism, owing to the unique structure and properties of the heterogeneous interfacial complexion (HIC) in the catalyst.

We also noticed that after electrolysis, the total N content decreased, and the N-W and N-O species decreased more than that of the N-W-O species **(Figure 4)**. The decrease of the N species is consistent to the observation of decreased NH_3 yield rate with extended electrolysis (**Figure S8**), which is commonly observed in TMN/TMN_xO_y based eNRR.[17] While the exact cause of the decreased NH_3 yield rate remains under investigation, the significant decrease in N-W species may suggest that re-filling the nitrogen vacancies (Nv) during eNRR may be still a limiting factor.[15,18,19] We hypothesize that a hybrid electrochemical and plasma system with in-situ plasma activation of N_2 would tackle this challenge, which is under intensive study currently.

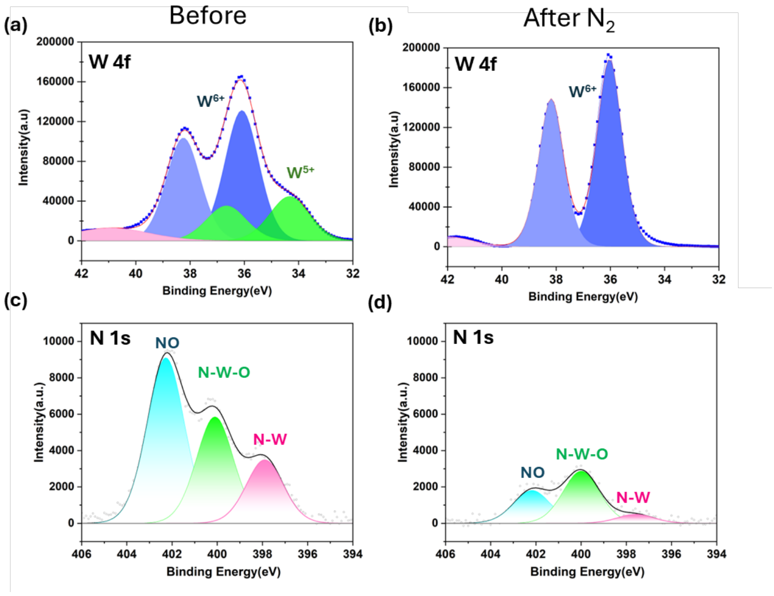

Figure 4. High-resolution XPS spectra of WO_xN_y/WO_3 catalyst before (a, c) and after (b, d) eNRR electrolysis for 3 hours in 5 mM H_2SO_4 electrolyte (pH = 2) under N_2.

In summary, this work developed a hybrid proton-intercalatable WO_xN_y/WO_3 electrochemical catalyst featuring a unique heterogeneous interfacial complexion (HIC) structure. This design enables facile in-situ electrochemical generation of active hydrogen atoms (H^*) in acidic electrolytes. The generated H^* facilitates both nitrogen hydrogenation and nitrogen vacancy (Nv) formation, enhancing the selectivity of the electrochemical nitrogen reduction reaction (eNRR) for ammonia synthesis while effectively suppressing the competing hydrogen evolution reaction (HER). A two-step fabrication process—combining microwave-assisted hydrothermal growth with plasma-assisted surface nitridation—was developed to synthesize the WO_xN_y/WO_3 heterogeneous interfacial catalyst. N_2/H_2 plasma was found to be more effective for surface nitridation than N_2 plasma alone or sequential H_2 and N_2 treatments, likely due to the formation of reactive NH_x radicals.

The HIC structured catalyst achieved a peak NH_3 yield rate of 3.2×10^{-10} $mol \cdot cm^{-2} \cdot s^{-1}$ with a Faradaic efficiency of 40.1%, outperforming most TMN/TMO_xN_y electrocatalysts, which typically exhibit FE<15%. Isotopic labeling and controlled experiments confirmed that the enhanced yield and FE originated from eNRR catalyzed by the WO_xN_y/WO_3 catalyst, proceeding via a MvK mechanism—referred to in this work as HIC enhanced MvK mechanism. Notably, the NH_3 yield rate was eight times higher and the FE approximately four times higher than that of a single-layer 2D W_2N_3 catalyst, despite the latter having significantly more accessible catalytic sites.[20] This suggests significant room for further performance improvements with thinner WO_xN_y/WO_3 nanosheets. Overall, this work advances the design and controllable fabrication of TMO/TMO_xN_y-based catalysts for enhanced eNRR activity and HER suppression.

ASSOCIATED CONTENT

Supporting Information

Supporting Information is available online free of charge.

Detailed information includes chemicals, experimental procedures for the fabrication and characterization of the catalysts, eNRR electrolysis setups including removing all possible contaminations in the N_2 feed and a novel setup for economically use the expensive $^{15}N_2$ gas in the ^{15}N isotope experiments, quantification of NH_4^+ via the indophenol blue method and NMR methods, and quantification of N_2H_4 via the Watt-Chrisp method.

AUTHOR INFORMATION

Corresponding Author

Yiguang Ju - *Department of Mechanical and Aerospace Engineering, Princeton University, Princeton, New Jersey 08544, United States; Princeton Plasma Physics Laboratory, Princeton, New Jersey 08543, United States*; Email: yju@princeton.edu

Huixin He - *Department of Chemistry, Rutgers, the State University of New Jersey, Newark, New Jersey 07102, United States*; Email: huixinhe@newark.rutgers.edu

Authors

Zhiyuan Zhang - *Department of Chemistry, Rutgers, the State University of New Jersey, Newark, New Jersey 07102, United States*

Christopher Kondratowicz - *Department of Mechanical and Aerospace Engineering, Princeton University, Princeton, New Jersey 08544, United States*

Jacob Smith - *Center for Nanophase Materials Sciences, Oak Ridge National Laboratory, Oak Ridge, Tennessee 37831, United States*

Pavel Kucheryavy - *Department of Chemistry, Rutgers, the State University of New Jersey, Newark, New Jersey 07102, United States*

Junjie Ouyang - *Department of Chemistry, Rutgers, the State University of New Jersey, Newark, New Jersey 07102, United States*

Yijie Xu - *Department of Mechanical and Aerospace Engineering, Princeton University, Princeton, New Jersey 08544, United States*

Sophia Kurdziel - *Applied Materials and Sustainability Sciences, Princeton Plasma Physics Laboratory, Princeton, New Jersey 08543, United States*

Eddie Tang - *Montgomery High School, Skillman, New Jersey 08558, United States; Department of Mechanical and Aerospace Engineering, Princeton University, Princeton, New Jersey 08544, United States*

Micheal Adeleke - *Science Park High School, Newark, New Jersey 07103, United States; Department of Chemistry, Rutgers, the State University of New Jersey, Newark, New Jersey 07102, United States*

Aditya Dilip Lele - *Department of Mechanical Engineering, Rowan University, Glassboro, New Jersey 08028, United States*

John Mark Martirez - *Applied Materials and Sustainability Sciences, Princeton Plasma Physics Laboratory, Princeton, New Jersey 08543, United States*

Miaofang Chi - *Thomas Lord Department of Mechanical Engineering & Materials Science, Duke University, Durham, North Carolina 27708, United States; Center for Nanophase Materials Sciences, Oak Ridge National Laboratory, Oak Ridge, Tennessee 37831, United States*

Notes

The authors declare no competing financial interest.

ACKNOWLEDGMENT

The collaborative effort of this study is supported by the US National Science Foundation (Award#: 2428523). HH would also like to acknowledge the support of Rutgers Research

Council. YJ would like to acknowledge the support from the DOE Plasma-Enhanced H_2 Production (PEHPr) Energy Earthshot Research Center (EERC) at Princeton Plasma Physics Laboratory under contract DEAC0209CH11466 for plasma reactors. Microscopy was partially conducted at the Center for Nanophase Materials Science, Oak Ridge National Laboratory, supported by the U.S. Department of Energy, Office of Science, and in part at the Analytical Instrumentation Facility (AIF) at NCSU, which is supported by the State of North Carolina and the National Science Foundation (award number ECCS-2025064). Participation of Princeton Plasma Physics Laboratory, a national laboratory operated by Princeton University for the U.S. Department of Energy under Prime Contract No. DE-AC02-09CH11466, is made possible via the Strategic Partnership Projects program.

References

(1) Shetty, A. U.; Sankannavar, R. Exploring nitrogen reduction reaction mechanisms in electrocatalytic ammonia synthesis: A comprehensive review. *Journal of Energy Chemistry* **2024**, *92*, 681-697. DOI: 10.1016/j.jechem.2024.01.024
(2) Peng, J.; Giner-Sanz, J. J.; Giordano, L.; Mounfield, W. P.; Leverick, G. M.; Yu, Y.; Román-Leshkov, Y.; Shao-Horn, Y. Design principles for transition metal nitride stability and ammonia generation in acid. *Joule* **2023**, *7* (1), 150-167. DOI: 10.1016/j.joule.2022.11.011
(3) Smith, C.; Hill, A. K.; Torrente-Murciano, L. Current and future role of Haber–Bosch ammonia in a carbon-free energy landscape. *Energy & Environmental Science* **2020**, *13* (2), 331-344. DOI: 10.1039/C9EE02873K
(4) Iriawan, H.; Andersen, S. Z.; Zhang, X.; Comer, B. M.; Barrio, J.; Chen, P.; Medford, A. J.; Stephens, I. E. L.; Chorkendorff, I.; Shao-Horn, Y. Methods for nitrogen activation by reduction and oxidation. *Nature Reviews Methods Primers* **2021**, *1* (1), 56. DOI: 10.1038/s43586-021-00053-y
(5) Fernández, C. A.; Chapman, O.; Brown, M. A.; Alvarez-Pugliese, C. E.; Hatzell, M. C. Achieving Decentralized, Electrified, and Decarbonized Ammonia Production. *Environmental Science & Technology* **2024**, *58* (16), 6964-6977. DOI: 10.1021/acs.est.3c10751
(6) Hatzell, M. C. The Colors of Ammonia. *ACS Energy Letters* **2024**, *9* (6), 2920-2921. DOI: 10.1021/acsenergylett.4c01391

(7) Gorky, F.; Lucero, J. M.; Crawford, J. M.; Blake, B. A.; Guthrie, S. R.; Carreon, M. A.; Carreon, M. L. Insights on cold plasma ammonia synthesis and decomposition using alkaline earth metal-based perovskites. *Catalysis Science & Technology* **2021**, *11* (15), 5109-5118. DOI: 10.1039/D1CY00729G

(8) Mehta, P.; Barboun, P.; Herrera, F. A.; Kim, J.; Rumbach, P.; Go, D. B.; Hicks, J. C.; Schneider, W. F. Overcoming ammonia synthesis scaling relations with plasma-enabled catalysis. *Nature Catalysis* **2018**, *1* (4), 269-275. DOI: 10.1038/s41929-018-0045-1

(9) Ju, Y.; Starikovskiy, A. *Plasma Assisted Combustion and Chemical Processing*; CRC press, 2025

(10) Qu, Z.; Zhou, R.; Sun, J.; Gao, Y.; Li, Z.; Zhang, T.; Zhou, R.; Liu, D.; Tu, X.; Cullen, P.; et al. Plasma-Assisted Sustainable Nitrogen-to-Ammonia Fixation: Mixed-phase, Synergistic Processes and Mechanisms. *ChemSusChem* **2024**, *17* (6), e202300783. DOI: 10.1002/cssc.202300783

(11) Sun, J.; Alam, D.; Daiyan, R.; Masood, H.; Zhang, T.; Zhou, R.; Cullen, P. J.; Lovell, E. C.; Jalili, A.; Amal, R. A hybrid plasma electrocatalytic process for sustainable ammonia production. *Energy & Environmental Science* **2021**, *14* (2), 865-872. DOI: 10.1039/D0EE03769A

(12) Zhang, T.; Zhou, R.; Zhang, S.; Zhou, R.; Ding, J.; Li, F.; Hong, J.; Dou, L.; Shao, T.; Murphy, A. B.; et al. Sustainable Ammonia Synthesis from Nitrogen and Water by One-Step Plasma Catalysis. *Energy & Environmental Materials* **2023**, *6* (2), e12344. DOI: 10.1002/eem2.12344

(13) Li, Q.; Kucukosman, O. K.; Ma, Q.; Ouyang, J.; Kucheryavy, P.; Gu, H.; Long, C. L.; Zhang, Z.; Young, J.; Lockard, J. V.; et al. Enhancement of Electrochemical Nitrogen Reduction Activity and Suppression of Hydrogen Evolution Reaction for Transition Metal Oxide Catalysts: The Role of Proton Intercalation and Heteroatom Doping, *ACS Catalysis* **2024**, *14* (11), 8899-8912. DOI: 10.1021/acscatal.4c00223

(14) Suryanto, B. H. R.; Du, H.-L.; Wang, D.; Chen, J.; Simonov, A. N.; MacFarlane, D. R. Challenges and prospects in the catalysis of electroreduction of nitrogen to ammonia. *Nature Catalysis* **2019**, *2* (4), 290-296. DOI: 10.1038/s41929-019-0252-4

(15) Deng, J.; Iniguez, J. A.; Liu, C. Electrocatalytic Nitrogen Reduction at Low Temperature. *Joule* **2018**, *2* (5), 846-856. DOI: 10.1016/j.joule.2018.04.014

(16) Abghoui, Y.; Skulason, E. Electrochemical synthesis of ammonia via Mars-van Krevelen mechanism on the (111) facets of group III-VII transition metal mononitrides. *Catalysis Today* **2017**, *286*, 78-84. DOI: 10.1016/j.cattod.2016.06.009

(17) Yang, X.; Nash, J.; Anibal, J.; Dunwell, M.; Kattel, S.; Stavitski, E.; Attenkofer, K.; Chen, J. G.; Yan, Y.; Xu, B. Mechanistic Insights into Electrochemical Nitrogen Reduction Reaction on Vanadium Nitride Nanoparticles. *Journal of the American Chemical Society* **2018**, *140* (41), 13387-13391. DOI: 10.1021/jacs.8b08379

(18) Ologunagba, D.; Kattel, S. Transition metal oxynitride catalysts for electrochemical reduction of nitrogen to ammonia. *Materials Advances* **2021**, *2* (4), 1263-1270. DOI: 10.1039/D0MA00849D

(19) Abghoui, Y.; Skúlason, E. Computational Predictions of Catalytic Activity of Zincblende (110) Surfaces of Metal Nitrides for Electrochemical Ammonia Synthesis. *The Journal of Physical Chemistry C* **2017**, *121* (11), 6141-6151. DOI: 10.1021/acs.jpcc.7b00196

(20) Abghoui, Y.; Garden, A. L.; Howalt, J. G.; Vegge, T.; Skúlason, E. Electroreduction of N2 to Ammonia at Ambient Conditions on Mononitrides of Zr, Nb, Cr, and V: A DFT Guide for Experiments. *ACS Catalysis* **2016**, *6* (2), 635-646. DOI: 10.1021/acscatal.5b01918

(21) Jin, H.; Li, L.; Liu, X.; Tang, C.; Xu, W.; Chen, S.; Song, L.; Zheng, Y.; Qiao, S.-Z. Nitrogen Vacancies on 2D Layered W_2N_3: A Stable and Efficient Active Site for Nitrogen Reduction Reaction. *Advanced Materials* **2019**, *31* (32), 1902709. DOI: 10.1002/adma.201902709

(22) Young, S. D.; Ceballos, B. M.; Banerjee, A.; Mukundan, R.; Pilania, G.; Goldsmith, B. R. Metal Oxynitrides for the Electrocatalytic Reduction of Nitrogen to Ammonia. *The Journal of Physical Chemistry C* **2022**, *126* (31), 12980-12993. DOI: 10.1021/acs.jpcc.2c02816

(23) Osonkie, A.; Ganesan, A.; Chukwunenye, P.; Anwar, F.; Balogun, K.; Gharaee, M.; Rashed, I.; Cundari, T. R.; D'Souza, F.; Kelber, J. A. Electrocatalytic Reduction of Nitrogen to Ammonia: the Roles of Lattice O and N in Reduction at Vanadium Oxynitride Surfaces. *ACS Applied Materials & Interfaces* **2022**, *14* (1), 531-542. DOI: 10.1021/acsami.1c16104

(24) Cui, L.; Sun, Z.; Wang, Y.; Jian, X.; Li, H.; Zhang, X.; Gao, X.; Li, R.; Liu, J. *H migration-assisted MvK mechanism for efficient electrochemical NH_3 synthesis over TM–TiNO. *Physical Chemistry Chemical Physics* **2024**, *26* (21), 15705-15716. DOI: 10.1039/D4CP01207K

(25) Yang, X. J.; Xu, B. J.; Chen, J. G. G.; Yang, X. Recent Progress in Electrochemical Nitrogen Reduction on Transition Metal Nitrides. *ChemSusChem* **2023**, *16* (5), e202201715. DOI: 10.1002/cssc.202201715

(26) Ye, T. N.; Park, S. W.; Lu, Y.; Li, J.; Sasase, M.; Kitano, M.; Hosono, H. Contribution of Nitrogen Vacancies to Ammonia Synthesis over Metal Nitride Catalysts. *Journal of the American Chemical Society* **2020**, *142* (33), 14374-14383. DOI: 10.1021/jacs.0c06624

(27) Ye, T.-N.; Park, S.-W.; Lu, Y.; Li, J.; Sasase, M.; Kitano, M.; Tada, T.; Hosono, H. Vacancy-enabled N_2 activation for ammonia synthesis on an Ni-loaded catalyst. *Nature* **2020**, *583* (7816), 391-395. DOI: 10.1038/s41586-020-2464-9

(28) Zhang, Z.; Feng, X.; Zhang, Z.; Chen, L.; Liu, W.; Tong, L.; Gao, X.; Zhang, J. Graphdiyne Enabled Nitrogen Vacancy Formation in Copper Nitride for Efficient Ammonia Synthesis. *Journal of the American Chemical Society* **2024**, *146* (21), 14898-14904. DOI: 10.1021/jacs.4c04985

(29) Dillon, S. J.; Tang, M.; Carter, W. C.; Harmer, M. P. Complexion: A new concept for kinetic engineering in materials science. *Acta Materialia* **2007**, *55* (18), 6208-6218. DOI: 10.1016/j.actamat.2007.07.029

(30) Kiafiroozkoohi, N. S.; Ghorbani, S. R.; Arabi, H.; Ghanbari, R. Electrochemical performance engineering of tungsten oxynitride by a nitrogen controlling synthesis method for a binder-free supercapacitor electrode. *Journal of Energy Storage* **2024**, *97*, 112956. DOI: 10.1016/j.est.2024.112956

(31) Chen, W. P.; He, K. F.; Wang, Y.; Chan, H. L. W.; Yan, Z. Highly mobile and reactive state of hydrogen in metal oxide semiconductors at room temperature. *Scientific Reports* **2013**, *3* (1), 3149. DOI: 10.1038/srep03149

(32) Yan, B.; Bisbey, R. P.; Alabugin, A.; Surendranath, Y. Mixed Electron–Proton Conductors Enable Spatial Separation of Bond Activation and Charge Transfer in Electrocatalysis. *Journal of the American Chemical Society* **2019**, *141* (28), 11115-11122. DOI: 10.1021/jacs.9b03327

(33) Miu, E. V.; McKone, J. R.; Mpourmpakis, G. The Sensitivity of Metal Oxide Electrocatalysis to Bulk Hydrogen Intercalation: Hydrogen Evolution on Tungsten Oxide. *Journal of the American Chemical Society* **2022**, *144* (14), 6420-6433. DOI: 10.1021/jacs.2c00825

(34) Ren, Y.; Yu, C.; Tan, X.; Wei, Q.; Wang, Z.; Ni, L.; Wang, L.; Qiu, J. Strategies to activate inert nitrogen molecules for efficient ammonia electrosynthesis: current status, challenges, and perspectives. *Energy & Environmental Science* **2022**, *15* (7), 2776-2805. DOI: 10.1039/D2EE00358A

(35) Ling, C.; Zhang, Y.; Li, Q.; Bai, X.; Shi, L.; Wang, J. New Mechanism for N_2 Reduction: The Essential Role of Surface Hydrogenation. *Journal of the American Chemical Society* **2019**, *141* (45), 18264-18270. DOI: 10.1021/jacs.9b09232

(36) Feng, X.; Liu, J.; Chen, L.; Kong, Y.; Zhang, Z.; Zhang, Z.; Wang, D.; Liu, W.; Li, S.; Tong, L.; et al. Hydrogen Radical-Induced Electrocatalytic N_2 Reduction at a Low Potential. *Journal of the American Chemical Society* **2023**, *145* (18), 10259-10267. DOI: 10.1021/jacs.3c01319

(37) Zhou, Y. Y.; Fu, X. B.; Chorkendorff, I.; Norskov, J. K. Electrochemical Ammonia Synthesis: The Energy Efficiency Challenge. *ACS Energy Letters* **2025**, *10* (1), 128-132. DOI: 10.1021/acsenergylett.4c02954

(38) Johnson, D.; Hunter, B.; Christie, J.; King, C.; Kelley, E.; Djire, A. Ti_2N nitride MXene evokes the Mars-van Krevelen mechanism to achieve high selectivity for nitrogen reduction reaction. *Scientific Reports* **2022**, *12* (1), 657. DOI: 10.1038/s41598-021-04640-7

(39) Nash, J.; Yang, X.; Anibal, J.; Dunwell, M.; Yao, S.; Attenkofer, K.; Chen, J. G.; Yan, Y.; Xu, B. Elucidation of the Active Phase and Deactivation Mechanisms of Chromium Nitride in the Electrochemical Nitrogen Reduction Reaction. *The Journal of Physical Chemistry C* **2019**, *123* (39), 23967-23975. DOI: 10.1021/acs.jpcc.9b05436

(40) Chang, B.; Deng, L.; Wang, S.; Shi, D.; Ai, Z.; Jiang, H.; Shao, Y.; Zhang, L.; Shen, J.; Wu, Y.; et al. A vanadium–nickel oxynitride layer for enhanced electrocatalytic nitrogen fixation in neutral media. *Journal of Materials Chemistry A* **2020**, *8* (1), 91-96. DOI: 10.1039/C9TA11378A

(41) Kang, S.; Wang, J.; Zhang, S.; Zhao, C.; Wang, G.; Cai, W.; Zhang, H. Plasma-etching enhanced titanium oxynitride active phase with high oxygen content for ambient electrosynthesis of ammonia. *Electrochemistry Communications* **2019**, *100*, 90-95. DOI: 10.1016/j.elecom.2019.01.028

(42) Gao, L.; Wang, X.; Xie, Z.; Song, W.; Wang, L.; Wu, X.; Qu, F.; Chen, D.; Shen, G. High-performance energy-storage devices based on WO_3 nanowire arrays/carbon cloth integrated electrodes. *Journal of Materials Chemistry A* **2013**, *1* (24), 7167-7173. DOI: 10.1039/C3TA10831G

(43) Huang, Z.; Yang, B.; Zhou, Y.; Luo, W.; Chen, G.; Liu, M.; Liu, X.; Ma, R.; Zhang, N. Tungsten Nitride/Tungsten Oxide Nanosheets for Enhanced Oxynitride Intermediate Adsorption and Hydrogenation in Nitrate Electroreduction to Ammonia. *ACS Nano* **2023**, *17* (24), 25091-25100. DOI: 10.1021/acsnano.3c07734

(44) Chen, Z.; Peng, Y. T.; Liu, F.; Le, Z. Y.; Zhu, J.; Shen, G. R.; Zhang, D. Q.; Wen, M. C.; Xiao, S. N.; Liu, C. P.; et al. Hierarchical Nanostructured WO_3 with Biomimetic Proton Channels and Mixed Ionic-Electronic Conductivity for Electrochemical Energy Storage. *Nano Letters* **2015**, *15* (10), 6802-6808. DOI: 10.1021/acs.nanolett.5b02642

(45) Kalanur, S. S.; Hwang, Y. J.; Chae, S. Y.; Joo, O. S. Facile growth of aligned WO_3 nanorods on FTO substrate for enhanced photoanodic water oxidation activity. *Journal of Materials Chemistry A* **2013**, *1* (10), 3479-3488. DOI: 10.1039/C3TA01175E

(46) Shi, J.; Pu, Z.; Liu, Q.; Asiri, A. M.; Hu, J.; Sun, X. Tungsten nitride nanorods array grown on carbon cloth as an efficient hydrogen evolution cathode at all pH values. *Electrochimica Acta* **2015**, *154*, 345-351. DOI: 10.1016/j.electacta.2014.12.096

(47) Dong, S.; Chen, X.; Zhang, X.; Cui, G. Nanostructured transition metal nitrides for energy storage and fuel cells. *Coordination Chemistry Reviews* **2013**, *257* (13), 1946-1956. DOI: 10.1016/j.ccr.2012.12.012

(48) Zhang, B.; Zheng, Y.; Xing, Z.; Wu, Z.; Cheng, C.; Ma, T.; Li, S. Interfacial electron-engineered tungsten oxynitride interconnected rhodium layer for highly efficient all-pH-value hydrogen production. *Journal of Materials Chemistry A* **2024**, *12* (8), 4484-4491. DOI: 10.1039/D3TA06856K

(49) Yang, X.; Zhao, F.; Yeh, Y. W.; Selinsky, R. S.; Chen, Z.; Yao, N.; Tully, C. G.; Ju, Y.; Koel, B. E. Nitrogen-plasma treated hafnium oxyhydroxide as an efficient acid-stable electrocatalyst for hydrogen evolution and oxidation reactions. *Nature Communications* **2019**, *10* (1), 1543. DOI: 10.1038/s41467-019-09162-5

(50) Liu, D.; Xu, Y.; Sun, M.; Huang, Y.; Yu, Y.; Zhang, B. Photothermally assisted photocatalytic conversion of CO_2–H_2O into fuels over a WN–WO_3 Z-scheme heterostructure. *Journal of Materials Chemistry A* **2020**, *8* (3), 1077-1083. DOI: 10.1039/C9TA10629D

(51) van Helden, J. H.; van den Oever, P. J.; Kessels, W. M. M.; van de Sanden, M. C. M.; Schram, D. C.; Engeln, R. Production Mechanisms of NH and NH_2 Radicals in N_2−H_2 Plasmas. *The Journal of Physical Chemistry A* **2007**, *111* (45), 11460-11472. DOI: 10.1021/jp0727650

(52) Liu, J.; Lu, H.; Zhang, D. W.; Nolan, M. Self-limiting nitrogen/hydrogen plasma radical chemistry in plasma-enhanced atomic layer deposition of cobalt. *Nanoscale* **2022**, *14* (12), 4712-4725. DOI: 10.1039/D1NR05568B

(53) Cong, S.; Yuan, Y. Y.; Chen, Z. G.; Hou, J. Y.; Yang, M.; Su, Y. L.; Zhang, Y. Y.; Li, L.; Li, Q. W.; Geng, F. X.; et al. Noble metal-comparable SERS enhancement from semiconducting metal oxides by making oxygen vacancies. *Nature Communications* **2015**, *6* (1), 7800. DOI: 10.1038/ncomms8800

(54) Hu, L.; Xing, Z.; Feng, X. Understanding the Electrocatalytic Interface for Ambient Ammonia Synthesis. *ACS Energy Letters* **2020**, *5* (2), 430-436. DOI: 10.1021/acsenergylett.9b02679

(55) Gebremariam, G. K.; Jovanović, A. Z.; Pašti, I. A. The Effect of Electrolytes on the Kinetics of the Hydrogen Evolution Reaction. *Hydrogen* **2023**, *4* (4), 776-806. DOI: 10.3390/hydrogen4040049

(56) Chen, J.; Chen, C.; Qin, M.; Li, B.; Lin, B.; Mao, Q.; Yang, H.; Liu, B.; Wang, Y. Reversible hydrogen spillover in Ru-$WO_{(3-x)}$ enhances hydrogen evolution activity in neutral pH water splitting. **2022**, *13* (1), 5382. DOI: 10.1038/s41467-022-33007-3

(57) Subbaraman, R.; Tripkovic, D.; Strmcnik, D.; Chang, K.-C.; Uchimura, M.; Paulikas, A. P.; Stamenkovic, V.; Markovic, N. M. Enhancing Hydrogen Evolution Activity in Water Splitting by Tailoring Li^+-$Ni(OH)_2$-Pt Interfaces. *Science* **2011**, *334* (6060), 1256-1260. DOI: 10.1126/science.1211934

(58) Choi, J.; Suryanto, B. H. R.; Wang, D.; Du, H.-L.; Hodgetts, R. Y.; Ferrero Vallana, F. M.; MacFarlane, D. R.; Simonov, A. N. Identification and elimination of false positives in electrochemical nitrogen reduction studies. *Nature Communications* **2020**, *11* (1), 5546. DOI: 10.1038/s41467-020-19130-z
(59) Du, H.-L.; Gengenbach, T. R.; Hodgetts, R.; MacFarlane, D. R.; Simonov, A. N. Critical Assessment of the Electrocatalytic Activity of Vanadium and Niobium Nitrides toward Dinitrogen Reduction to Ammonia. *ACS Sustainable Chemistry & Engineering* **2019**, *7* (7), 6839-6850. DOI: 10.1021/acssuschemeng.8b06163
(60) Manjunatha, R.; Karajić, A.; Teller, H.; Nicoara, K.; Schechter, A. Electrochemical and Chemical Instability of Vanadium Nitride in the Synthesis of Ammonia Directly from Nitrogen. *ChemCatChem* **2020**, *12* (2), 438-443. DOI: 10.1002/cctc.201901558.
(61) Hu, B.; Hu, M.; Seefeldt, L.; Liu, T. L. Electrochemical Dinitrogen Reduction to Ammonia by Mo_2N: Catalysis or Decomposition? *ACS Energy Letters* **2019**, *4* (5), 1053-1054. DOI: 10.1021/acsenergylett.9b00648

Supporting Information for

Plasma Assisted Surface Nitridation of Proton Intercalatable WO_3 for Efficient Electrocatalytic Ammonia Synthesis

Zhiyuan Zhang [a], *Christopher Kondratowicz* [b], *Jacob Smith* [c], *Pavel Kucheryavy* [a], *Junjie Ouyang* [a], *Yijie Xu* [b], *Elizabeth Desmet* [b], *Sophia Kurdziel* [d], *Eddie Tang* [b, e], *Micheal Adeleke* [a, f], *Aditya Dilip Lele* [g], *John Mark Martirez* [d], *Miaofang Chi* [c, h], *Yiguang Ju* [b, d*], *Huixin He* [a]*

[a] Department of Chemistry, Rutgers, the State University of New Jersey, Newark, New Jersey 07102, United States

[b] Department of Mechanical and Aerospace Engineering, Princeton University, Princeton, New Jersey 08544, United States

[c] Center for Nanophase Materials Sciences, Oak Ridge National Laboratory, Oak Ridge, Tennessee 37831, United States

[d] Applied Materials and Sustainability Sciences, Princeton Plasma Physics Laboratory, Princeton, New Jersey 08543, United States

[e] Montgomery High School, Skillman, New Jersey 08558, United States

[f] Science Park High School, Newark, New Jersey 07103, United States

[g] Department of Mechanical Engineering, Rowan University, Glassboro, New Jersey 08028, United States

[h] Thomas Lord Department of Mechanical Engineering & Materials Science, Duke University, Durham, North Carolina 27708, United States

S1. Fast fabrication of WO_3 nanosheet array on carbon cloth with the microporous layer (MPL) via a microwave hydrothermal method

A microwave hydrothermal method was applied to fabricate the WO_3 nanosheet array directly on a carbon cloth support with the microporous layer (MPL). The recipe for the fabrication was slightly modified from the work by Gao *et al*[1]. In brief, 1.25 mmol of sodium tungstate dihydrate ($Na_2WO_4 \cdot 2H_2O$) was dissolved in deionized water (10 mL) under vigorous stirring for 20 min. Subsequently a 3M HCl aqueous solution was slowly dropped into the solution until the pH value of the solution reached 1.2 to form a yellowish transparent solution. Then, 3.5 mmol oxalic acid ($H_2C_2O_4$) was added into the above mixture and diluted to 25 mL, which resulted in the formation of the $H_2C_2O_4$ precursor. For the next step, the as-prepared 4 mL H_2WO_4 precursor was transferred into a microwave tube, and then 0.1 g of Na_2SO_4 was added to the solution to control the structure. A piece of carbon cloth (0.75cm × 0.75 cm in size) with the MPL (Hydro-LAT 1400, Fuel Cells ETC), which was ultrasonically cleaned by deionized water and alcohol in sequence, was put into the microwave tube and sealed, and maintained at 180 °C for 15 minutes by microwave oven (Discover SP, CEM). After the autoclave cooled down to room temperature, the WO_3 membrane was taken out and rinsed with deionized water several times and dried at 70 °C in ambient.

S2. Plasma assisted surface nitridation of the WO_3 nanosheet array

The as-fabricated WO_3 nanosheet arrays on carbon cloth support were treated with 16-torr N_2 and N_2/H_2 plasma for different durations, as specified in the sample names. The plasma was generated in a home-made DBD cell, powered by a 20-kHz, 13-kV AC power supply. After plasma treatment, the composition, oxidation states, and morphology of the samples were analyzed by a range of surface characterization techniques, including X-ray photoelectron spectroscope (XPS), scanning electron microscope (SEM) and high-angle annular dark-field scanning transmission electron microscopy (HAADF-STEM).

S3. Characterization of the Electrocatalysts

The morphology of the WO_3 and WO_xN_y/WO_3 was analyzed by field emission scanning electron microscope (FE-SEM) (Hitachi S-4800 and JSM-7900F, JEOL, Japan) at 15 kV. The crystalline structures were investigated by X ray diffraction (XRD, a Rigaku Miniflex 6G) with a Co Ka radiation (λ = 1.789 Å). The surface chemical states and compositions were measured by X-ray photoelectron spectroscope (XPS, Thermo, K-Alpha, USA) with a monochromatic Al Kα radiation (hv = 1486.6 eV). All spectra were calibrated using the binding energy of C 1s (284.8 eV) as a reference.

High-angle annular dark-field scanning transmission electron microscopy (HAADF-STEM) was acquired on an aberration-corrected JEOL NEOARM operating at 200 kV using a convergence semi-angle of 28 mrad. Any electron energy loss spectroscopy (EELS) data was acquired on an aberration corrected FEI Titan microscope operating at 300 kV using a convergence semi-angle of 19.3 mrad. A 0.1 eV/channel dispersion was used during dual EELS data acquisition, wherein the low loss contains the zero-loss peak and the high loss contains both the O K-edge and N K-edge simultaneously. A full-width half maximum of the zero-loss peak registers an energy resolution of 1.0 eV. STEM samples were prepared using a solution-casting technique. The initial sample powders were dispersed in isopropyl alcohol and sonicated. Thereafter, the solution was applied to conventional lacey carbon TEM foil grids.

S4. Assessment of eNRR performance of the WO_xN_y/WO_3 hybrid catalyst electrodes

All the electrochemical measurements were performed using a CHI 760 C Potentiostat (CH Instruments, USA). Ag/AgCl (sat. KCl) and Pt wire were used as reference (RE) and counter electrodes (CE), respectively. The applied potentials measured against the Ag/AgCl reference electrode in saturated KCl were converted to the reversible hydrogen electrode (RHE) using the equation:

$$\mathrm{RHE} = E_{\mathrm{Ag/AgCl}} + 0.197\ \mathrm{V} + 0.059\times\mathrm{pH} \qquad \text{(eq1)}$$

S5. eNRR setup

The eNRR performance of the WO_xN_y/WO_3 hybrid catalyst electrodes was evaluated using a CH Instruments 760E Potentiostat with a homemade designed N_2 flow electrolysis cell as shown in **Scheme S1a.** This cell consists of a proton exchange membrane (Nafion 117, Dupont), a piece of Pt plate, Ag/AgCl (saturated KCl) electrode, which act as the counter electrode (CE), and reference electrode, respectively. The working electrode (WE) is the as-prepared WO_xN_y/WO_3 hybrid catalyst electrodes with a size of 0.7 × 0.7 cm, which were directly used as a catalytic gas-diffusion electrode (GDE) for eNRR to alleviate the low solubility issue of N_2 in water-based electrolytes (0.71 mg/mL). To eliminate potential NO_x and NH_3 contamination in the N_2 gas, pressurized N_2 (flow rate: 2.5 mL/min) from the gas tank was passed through three traps arranged in series before being introduced to the backside of the GDE (the side without catalyst coating) for eNRR **(Scheme S1b)**. The three purification traps included: (1) A $KMnO_4$ oxidation trap to oxidize any NO_3 present in the N_2 gas into soluble NO_3^-. (2) A KOH trap to remove the possibly formed NO_3^-. (3) A 0.1 M H_2SO_4 solution to trap any residual NH_3 in the N_2 gas. After purification, the N_2 gas was purged onto the backside of the GDE to initiate eNRR and the excess gas was purged back to the electrolyte to avoid the loss of the produced NH_3 carried over by the N_2 flow during the eNRR. The WE side and the CE side were separated by a Nafion 117 membrane (Fuel cell store). The electrolysis was performed for 0.5 h with constant potential in a H_2SO_4 solution (pH = 2) as the electrolyte. The electrolyte in the WE side of the cell was collected for ammonium (NH_3) and hydrazine (N_2H_4) detection using the indophenol blue UV-Vis spectroscopy method and NMR spectroscopy as detailed **in sections S6-8.** The NH_3 yield rate and the Faradic efficiency for the nitrogen-ammonia conversion were calculated as detailed in **section S9.**

S6. Determination of NH_4^+ via the indophenol blue method

The concentration of the produced NH_4^+ was spectrophotometrically determined by the indophenol blue method. Typically, 1 mL of electrolyzed electrolyte was transferred from the electrochemical cell to a clean vial. Then 1 mL of solution containing 1M NaOH with 5 wt% salicylic acid and 5 wt% sodium citrate was added to the vial. Then 0.5 mL of 5 wt% NaClO aqueous solution and 0.1 mL of 1 wt% sodium nitroprusside solution was sequentially dropwise added to the mixture. After reacting for 2 h, the UV-vis spectrum was collected from 750 nm to 500 nm. Calibration curve was made using NH_4Cl standard (BTC) diluted to 0.4, 0.8, 1.2, 1.6 ppm (NH_4^+ concentration) with the fresh electrolyte. Calibration curve was made at each time the electrolyzed electrolytes were measured.

S7. Determination of N_2H_4

N_2H_4 was determined by Watt and Chrisp colorimetric method. In brief, the color reagent was obtained by mixing concentrated HCl (30 mL), C_2H_5OH (300 mL) and $C_9H_{11}NO$ (5.99 g). And 5 mL electrolyte was taken from the cathodic chamber and added into 5 mL above as-prepared color reagent. After standing for 15 minutes, the absorption spectrum of the solution was collected in the wavelength range of 420-500 nm, and the peak appears at 455 nm. The calibration curve was measured using the absorbance of N_2H_4 solution with different concentrations. Calibration curve displays good linear relationship of absorbance with N_2H_4 concentrations ($y = 1.0158x + 0.1519$, $R^2 = 0.9991$) by taking the mean of three times independent calibration.

S8. $^{15}N_2$ isotope label experiment and NMR Analysis:

Before starting the nitrogen reduction reaction (NRR) experiment using ^{15}N-labeled nitrogen, the system was purged with argon gas three times over a total of 30 minutes to remove any residual air. After purging, the argon supply was turned off, and the balloon was evacuated by pump before being filled with $^{15}N_2$ gas. The electrolysis was then conducted at -0.15 V vs RHE for 30 minutes. Following electrolysis, the electrolyte was collected for further analysis of the ^{15}N-labeled products.

For NMR sample preparation, the pH of the electrolyte was adjusted to 4.5, maleic acid was added as an internal standard, and DMSO-d_6 was used to lock the sample. NH_4^+ detection via NMR was performed using the excitation sculpting water suppression (zgesgp pulse sequence) on a Bruker 500 MHz Avance III HD spectrometer. To improve the signal-to-noise ratio, the following parameters were optimized: frequency offset (O1P), size of the free induction decay (FID) (TD), pre-scan delay (D1), and the number of scans (NS). While O1P varied from experiment to experiment, TD was set to 16,378, D1 to 1 s, and NS to 16,378.

Before starting the NRR experiment using ^{15}N-labeled nitrogen, the system was purged with argon gas three times over a total of 30 minutes to remove residual air. Afterward, the argon supply was shut off, and the balloon was evacuated by pump and subsequently filled with $^{15}N_2$ gas. The electrolysis was then carried out at -0.15V vs RHE for 30 minutes. Finally, the electrolyte was collected for further analysis of the ^{15}N-labeled products. NMR samples were prepared in the particular way: after electrolysis pH was adjusted to 4.5, maleic acid was added as internal standard, and DMSO-d6 to lock. NH_4^+ detection via NMR was performed using the excitation sculpting water suppression (zgesgp pulse sequence) on Bruker 500 MHz Avance III HD spectrometer. For better signal-to-noise ratio the following parameters were optimized: frequency offset (O1P), size of FID (TD), pre-scan delay (D1), and number of scans (NS). While O1P was varied from experiment-to-experiment TD was set to 16378, D1 to 1 s, and NS to 16378.

S9. Calculation of NH_3 yield rate and Faradic efficiency for ammonia production

The NH_3 yield rate was calculated by Eq. (S2)

$$R_{NH_3} = \frac{C[NH_4^+] \times V}{s_{cat} \times t} \qquad \text{(eq2)}$$

where $C[NH_4^+]$ is the concentration of $[NH_4^+]$ in the electrolyte in the WE side, V is the volume of the electrolyte, S_{cat} is the catalyst electrode area, t is the electrolysis duration.

The Faradic efficiency for the nitrogen-ammonia conversion was calculated by Eq. (S3):

$$FE = \frac{3 \times C[NH_4^+] \times V \times F}{Q} \qquad \text{(eq3)}$$

where Q is the total charge passed during the electrolysis, F is Faraday constant (96485 C mol^{-1}).

S10. Estimation of electrochemical surface areas (ECSAs) of the catalysts

To ensure consistent WO_3 coverage—and thus identical surface areas—across all electrodes when assessing the impact of nitrogen content, every sample was deposited on a 0.5 cm^2 geometric area and prepared under strictly controlled microwave conditions. The resulting products were carefully characterized using SEM and the double-layer capacitance (C_{dl}) method to ensure a consistent density of WO_3 nanosheets on the carbon cloth support. The C_{dl} method was used to estimate the ECSA of the WO_3 catalysts before and after nitridation. As shown in Figure **S4**, nonpolarized cyclic voltammetry (CV) was performed in the range of 0.30–0.40 V vs RHE. The C_{dl} of each WO_3 sample before nitridation is consistently around 1.51 mF cm^{-2}, while the C_{dl} for WO_3-H_2/N_2-2h increased slightly to 2.02 mF cm^{-2}. This increase may be attributed to its higher conductivity and surface amorphization, as seen in the TEM image. Nevertheless, this minor change in C_{dl} suggests that the ECSA change is negligible compared to the significant enhancement in NRR activity. Therefore, we conclude that the surface areas of the electrodes are similar, and the observed performance differences are primarily due to nitrogen incorporation rather than surface area effects.

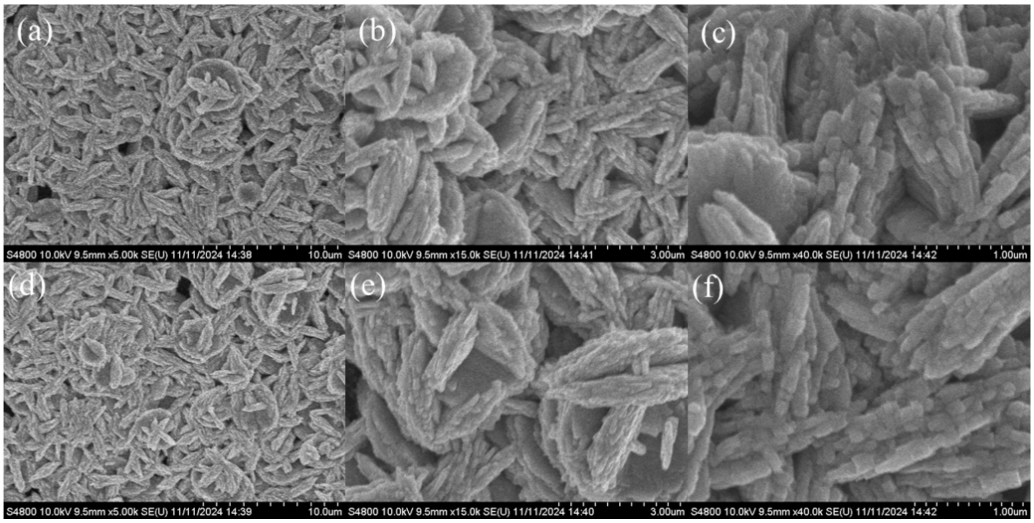

Figure S1. (a, b and c) Typical SEM images of h-WO_3 at different magnifications. (d, e and f) Typical SEM images of WO_3-H_2/N_2-2h with the same magnifications as in a-c for comparison.

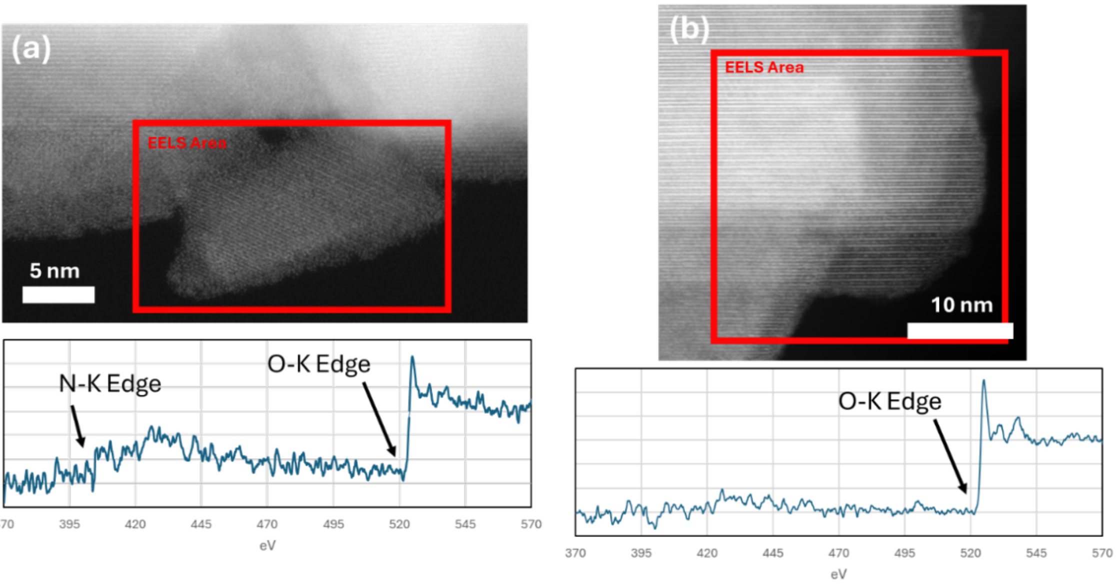

Figure S2. Observing surface nitridation of WO_3 after plasma treatment using EELS. (a) N-rich regions of WO_3 are evident by the presence of severe surface reconstruction. By comparison, (b) minimal N-signal is observed when bulk WO_3 EELS signals dominate the spectra.

Table S1. XPS quantification of the deconvoluted peaks shown in **Figure 2**.

Sample	W at%	O at%	N at%	$N_{(N\text{-}W)}/N_{total}$ (%)
WO_3-H_2/N_2-2h	25.2	60.5	14.3	19
WO_3-H_2/N_2-1h	23.5	65.5	10.8	12
WO_3-N_2-1h	23.9	68.5	7.6	0
WO_3-H_2-0.5h-N_2-1h	23.1	66.7	10.2	0

at%: Atomic Percentage

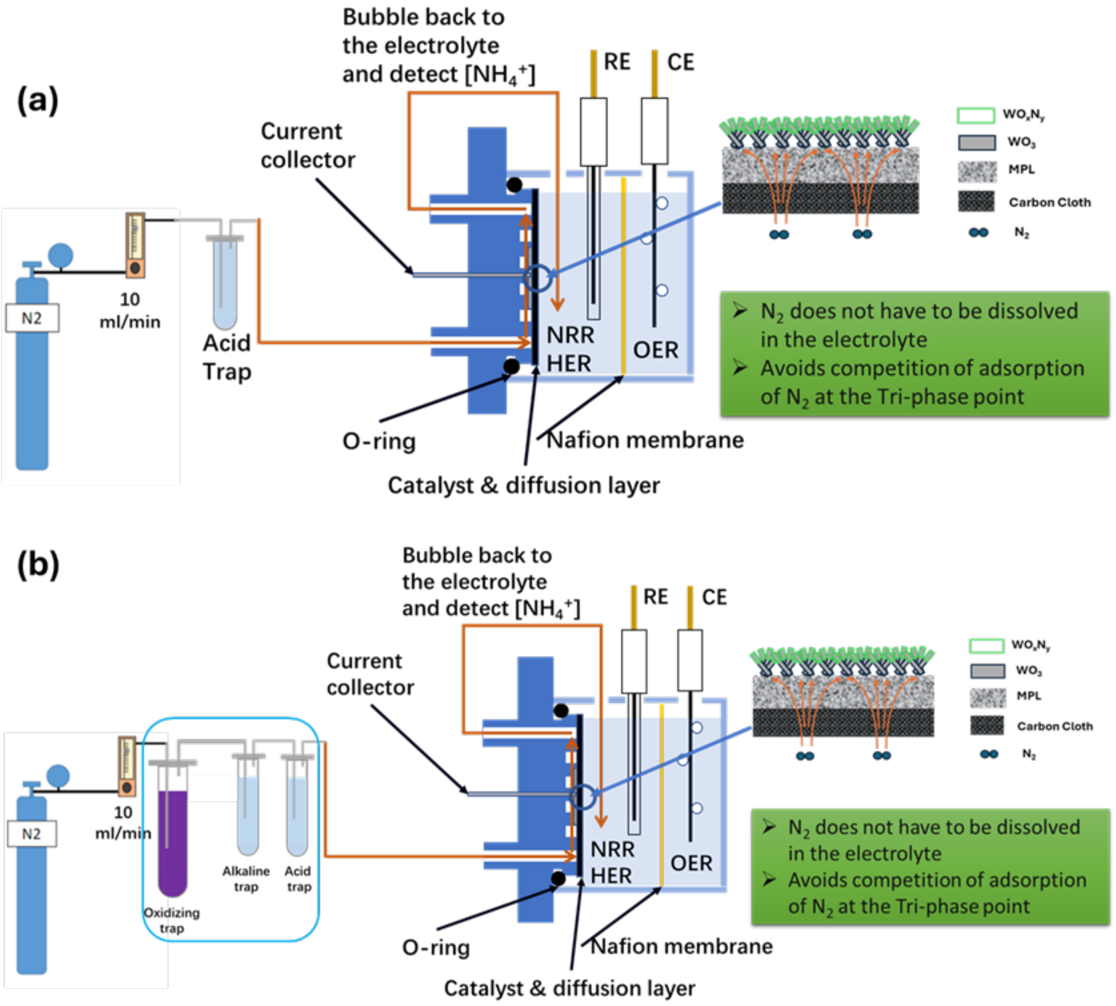

Scheme S1. Schematic drawings to show the (a) set-up for the eNRR electrolysis. (b) NO_x control set-up: any NO_x breakthrough from the oxidizing trap (filled with 0.1 M $KMnO_4$ in aqueous 0.1 M KOH) is captured by an alkaline trap (filled with aqueous 0.1 M KOH). All NH_3 breakthroughs and alkaline solutions will be captured by the acid trap (filled with concentrated H_2SO_4).

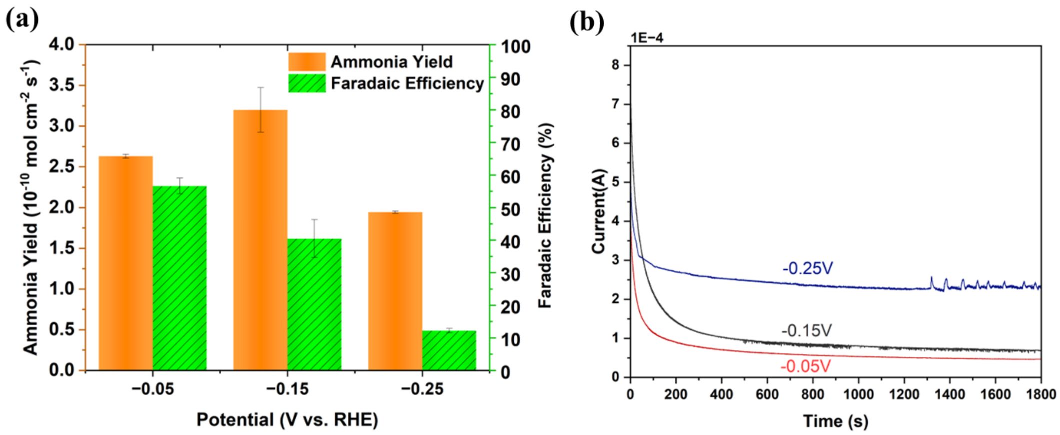

Figure S3. (a) Specific yield rate and faradaic efficiency of WO_3-H_2/N_2-2h at different cathodic potentials. (b) Chronoamperometry curves of WO_3-H_2/N_2-2h catalyst at different potentials for 30 min in pH = 2 H_2SO_4 electrolyte.

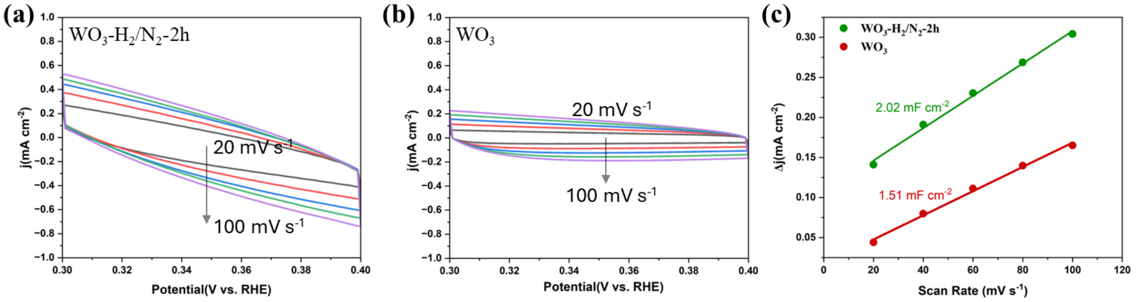

Figure S4. Cyclic voltammetry (CV) curves at the non-Faraday reaction region with different scanning rates (a) WO_3-H_2/N_2-2h, (b)WO_3. (c) The current density at 0.35V as a function of scanning rates of the CVs. The C_{dl} of the WO_3-H_2/N_2-2h and WO_3 were estimated by the slopes.

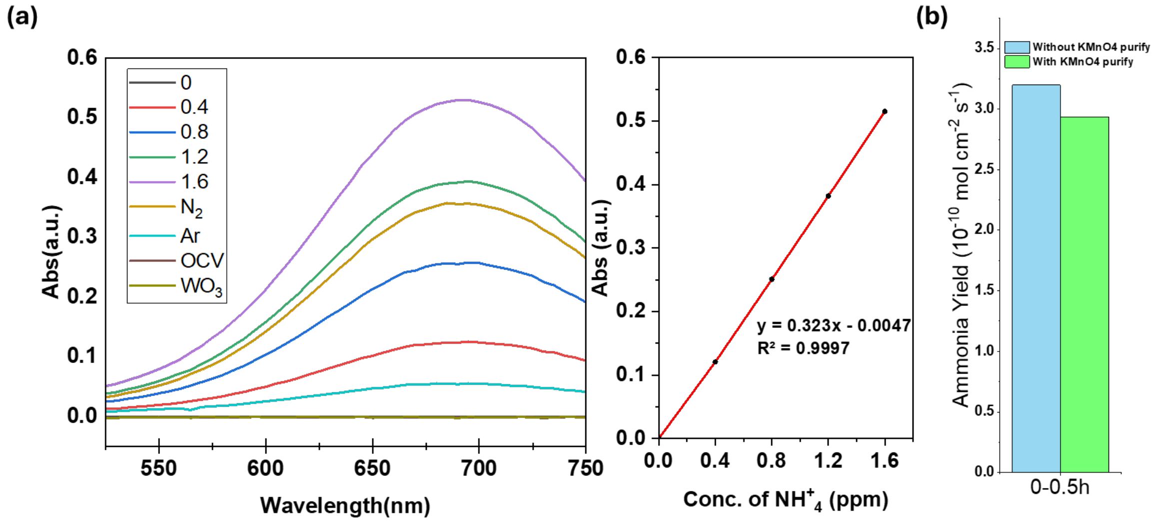

Figure S5. (a) UV–vis spectra of the electrolytes collected from the various control experiments following the indophenol blue spectrophotometric method. (b) comparison of NH_3 yield rate with/without NO_x removal from the N_2 feed.

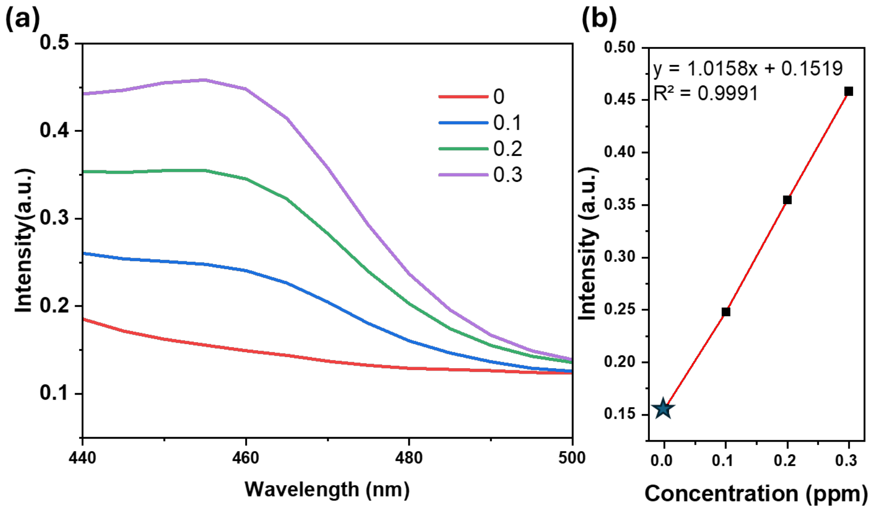

Figure S6. (a) UV-VIS spectra of various N_2H_4 concentrations after incubated for 15 min at room temperature. (b) Calibration curve used for calculation of N_2H_4 concentrations.

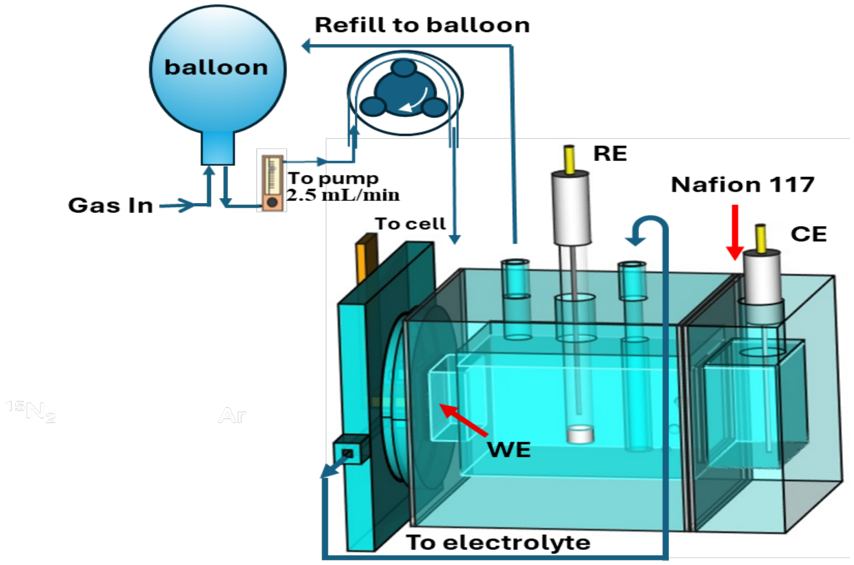

Scheme S2. Schematic drawings to show the set-up for the $^{15}N_2$ isotope eNRR electrolysis.

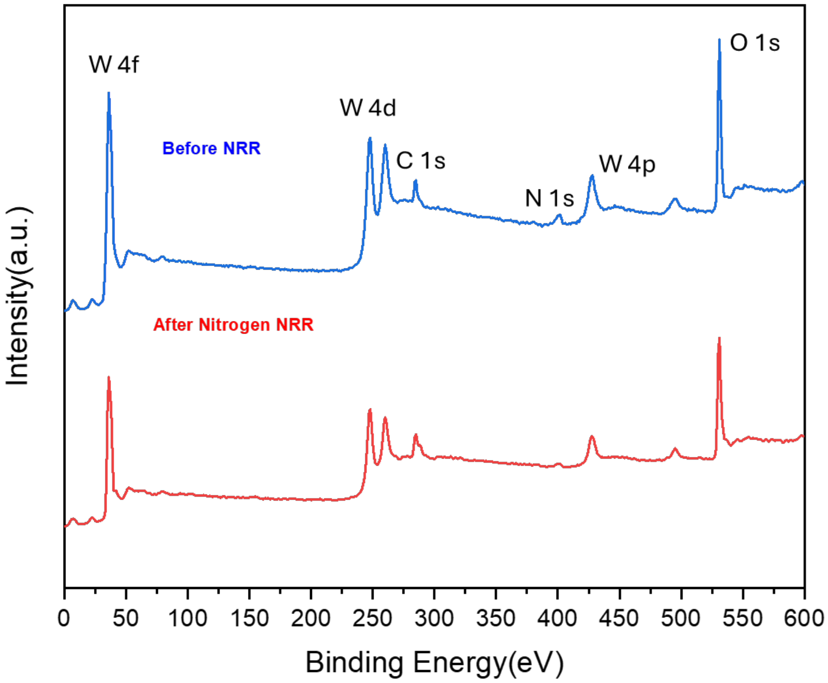

Figure S7. XPS spectra of WO_3/WO_xN_y before and after NRR.

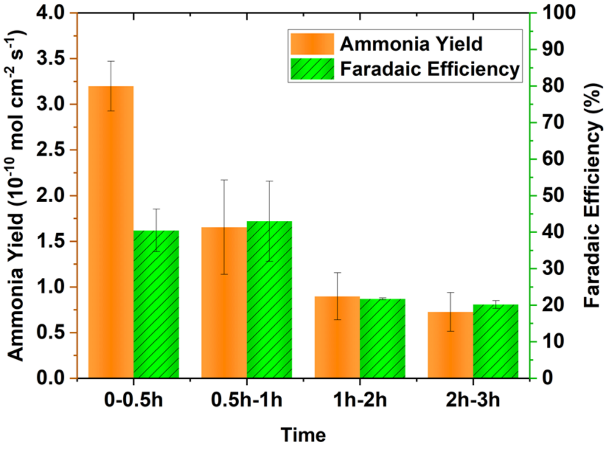

Figure S8. Specific yield rate and faradaic efficiency of WO_3-H_2/N_2-2h at -0.15V in three hours cycle.

Reference:

(1) Gao, L.; Wang, X.; Xie, Z.; Song, W.; Wang, L.; Wu, X.; Qu, F.; Chen, D.; Shen, G. High-performance energy-storage devices based on WO_3 nanowire arrays/carbon cloth integrated electrodes. *Journal of Materials Chemistry A* **2013**, *1* (24), 7167-7173. DOI: 10.1039/C3TA10831G